Time-lapse waveform analysis for elastic and anelastic structural changes of transducer-transducer active seismic experiments' data during triaxial deformation of granitic rock

Ssu-Ting Lai[1], Nobuaki FUJI[1], Ikuo Katayama[2], Luis Fabian Bonilla[3], and Yann Capdeville[4]

[1]Institut De Physique Du Globe De Paris
[2]Hiroshima University
[3]Université Gustave Eiffel
[4]Université de Nantes

November 21, 2022

Abstract

We quantitatively evaluate transducer-transducer one-source one-station active seismic waveform data, in order to monitor time-lapse changes of elastic and anelastic structure during deformation experiments in laboratory. The experiment data of dry and water-saturated sample are provided by Zaima and Katayama (2018, https://doi.org/10.1029/2018JB016377). A transducer receiver, at the mid-point of cylindrical rock sample, is located on the antipodal position of the transducer source, emitting compressional and shear waves. Due to the extremely underdetermined nature of inverse problem, we limit the number of unknowns to be four: global P- and S- wave velocities and their corresponding anelastic attenuation factors, which can represent the micro-cracks nucleation during the loading and before the appearance of the largest crack that causes the fracture. We first performed a trial-and-error search for a realistic boundary condition in three-dimensional seismic waveform modeling using spectral-element method, in order to fit the synthetic data with the observed waveforms. We then generated synthetic data for 6000 combinations of elastic and anelastic parameters, in order to conduct Monte-Carlo waveform inversion based on the cost functions using waveform misfit and zero-lag cross-correlation. We obtained the time-lapse changes in velocity and attenuation during the deformation, which are then linked to crack development. Compared with the wet experiment, the dry experiment has a larger change in both the velocity and attenuation. However, regardless of the configuration, global seismic wave speeds rise first and then decrease during the experiments. The quality factor shows roughly the same trend.

Time-lapse waveform analysis for elastic and anelastic structural changes of transducer-transducer active seismic experiments' data during triaxial deformation of granitic rock

Ssu-Ting Lai[1], Nobuaki Fuji[1], Ikuo Katayama[2], Luis Fabian Bonilla[1,3], Yann Capdeville[4]

[1]Institut de physique du globe de paris, Université de Paris, CNRS, F-75005 Paris, France
[2]Department of Earth and Planetary Systems Science, Hiroshima University, Higashi-Hiroshima, Japan
[3]Université Gustave Eiffel, Cité Descartes, 77447 Marne-la-Vallée Cedex 2, France
[4]Laboratoire de Planétologie et de Géodynamique de Nantes, Nantes, France

Key Points:

- numerical modeling
- triaxial experiment
- inverse theory
- weakening and rupture processes
- synthetic seismogram

Abstract

We quantitatively evaluate transducer-transducer one-source one-station active seismic waveform data, in order to monitor time-lapse changes of elastic and anelastic structure during deformation experiments in laboratory. The experiment data of dry and water-saturated sample are provided by Zaima and Katayama (2018, https://doi.org/10.1029/2018JB016377). A transducer receiver, at the mid-point of cylindrical rock sample, is located on the antipodal position of the transducer source, emitting compressional and shear waves. Due to the extremely underdetermined nature of inverse problem, we limit the number of unknowns to be four: global P- and S- wave velocities and their corresponding anelastic attenuation factors, which can represent the micro-cracks nucleation during the loading and before the appearance of the largest crack that causes the fracture. We first performed a trial-and-error search for a realistic boundary condition in three-dimensional seismic waveform modeling using spectral-element method, in order to fit the synthetic data with the observed waveforms. We then generated synthetic data for 6000 combinations of elastic and anelastic parameters, in order to conduct Monte-Carlo waveform inversion based on the cost functions using waveform misfit and zero-lag cross-correlation. We obtained the time-lapse changes in velocity and attenuation during the deformation, which are then linked to crack development. Compared with the wet experiment, the dry experiment has a larger change in both the velocity and attenuation. However, regardless of the configuration, global seismic wave speeds rise first and then decrease during the experiments. The quality factor shows roughly the same trend.

1 Introduction

In order to understand the earthquake nucleation, it is indispensable to study both the macroscopic and microscopic behaviors of the rupture process of the Earth's crust and mantle by global-scale numerical modeling (Fliss et al., 2005; Gabriel et al., 2012), natural earthquakes observation (Di Carli et al., 2010; Lee et al., 2011) and laboratory experiments of rock samples (Lockner et al., 1977; Toksöz et al., 1979; Guéguen & Schubnel, 2003; Benson et al., 2006). Averaged elastic wave velocities of a loaded rock sample could represent the localized nucleation and the growth of cracks, understanding the time-lapse changes of the deformation of experimental rock will lead us to the insight of the earthquake generation process (Scholz et al., 1973). Zaima and Katayama (2018) performed triaxial compression experiment on Aji granite and studied the evolution of elastic wave velocities and seismic amplitude during rock deformation. This experiment reveals that the compressional wave velocity (V_P) and the shear wave velocity (V_S) first increase due to the closure of the micro-cracks oriented normally to the maximum compression stress and then decrease due to the growth of the cracks aligned parallel with the compression stress when approach the failure. Similar features have been observed in various types of crystalline rocks (e.g., Scott et al., 1993; Guéguen & Schubnel, 2003; Paterson & Wong, 2005; S. Stanchits et al., 2006).

Möllhoff et al. (2010) simulated the preexisting artificial fracture in the rock using 2D discrete elastic lattice method, whereas Lai et al. (2019) studied the velocity model changes during rock deformation using the 2D finite differences method. However, 2D numerical modeling is insufficient to describe wave propagation in a 3D rock, even though the transfer function Lai et al. (2019) or 2D line source approximation seems to be functioning to some extent (Igel et al., 2002). On the other hand, some recent efforts of 3D numerical modeling of seismic waveforms in a laboratory scale are promising despite a number of difficulties. Yoshimitsu et al. (2016) modeled the geometry effect on cylindrical aluminum using 3D finite difference method, for a cylinder with 5 cm diameter and 10 cm height with a dominant frequency between 200 kHz-800 kHz. Solymosi et al. (2018) presented an excellent waveform fit using spectral element method on plastic water tank, for 60 cm $\times$ 40 cm scale with a dominant frequency of 500 kHz. Their comparisons between synthetics and observed data, being limited to homogeneous metals and plastics experiments, has shown the feasibility of numerical reproducibility of active seismic laboratory experiments. Brantut (2018) monitored acoustic emission on small-scaled sandstone using a 3D fast-marching method with finite differences and concomitantly constructed the evolution of velocity changes of the rock during its deformation inferred from the inversion. This study is encouraging due to the treatment of time-lapse data. The present work extends the idea to carefully treat not only the first arrivals but the entire waveforms and later phases in order to extract information on attenuation.

The aim of this study is to invert the seismic data with the aid of numerical modeling, instead of handpicking traveltimes of active transducer-transducer active seismic data for elastic structural changes as performed by Zaima and Katayama (2018). The idea is to robustly and quantitatively infer the subtle structural changes of anelasticity as well as elasticity, and three-dimensional structure in the near future. There are little number of previous studies that attempted "waveform inversion" of laboratory experiments. We use the spectral-element method (SEM) (Komatitsch & Vilotte, 1998; Chaljub et al., 2007) to model wave propagation in a rock sample during deformation. The spectral-element method can accurately handle the boundary condition in 3D complex models (Capdeville et al., 2003; Peter et al., 2011; De Basabe & Sen, 2014) (Chaljub et al., 2015). However, due to its computational costs, there are only few studies devoted to the comparison of SEM synthetics with laboratory experimental data (e.g., Pageot et al., 2017; Solymosi et al., 2018). Here, we perform SEM modeling on one-source and one-receiver experimental data, in order to show the adaptability of SEM to the seismic data for rock samples in laboratory. Throughout 3D simulation, we systematically construct a database of waveforms for models of different sets of globally constant elastic and anelastic parameters: V_P, V_S, Q_P, Q_S. We then perform Monte-Carlo waveform inversion using an objective function which combines with three kinds of cost functions: l_1-norm and l_2-norm of waveform misfit and zero-lag cross-correlation. We would like to explore knowledge of rock elastics and attenuation changes using numerical simulation and Monte-Carlo inversion. Our approach will show how numerical models help understand the observations and illustrate seismic characteristic of rock deformation.

2 Data and Methods

In order to perform an inversion in order to image elastic and anelastic structural changes during the rock deformation, we first acquire the active seismic data during the deformation experiment, while preparing a set of synthetic seismograms with the aid of spectral-element method. We then select the preferred models for an individual set of observed seismograms (measured as compressional and shear strains) for each differential stress step, in order to obtain the time-lapse trend of elastic and anelastic structure. Therefore, we were performing Monte-Carlo waveform inversion through the study. Here in this section, we first revisit briefly the experiment configurations and describe the robust information and unknown parameters (source and transfer function). Second, we describe the numerical modeling scheme and finally present our data processing strategy based on the data and modeling conditions. Then, we detail the idea of inverse problem implemented in this study.

2.1 Experimental setup

Triaxial compression experiments apply a confining pressure to a cylindrical rock sample wrapped in an impervious membrane, and then loads it axially to failure with dynamic compression. Zaima and Katayama (2018) conducted triaxial compression experiment on Aji granite, which mainly contains quartz, plagioclase, potash feldspar and biotite with an average grain size of about 0.3 mm (Kudo et al., 1992), and this study is based on both the dry and wet experiments. The wet experiment is under fluid-saturated condition, where distilled water is used as a pore fluid. The pore pressure of wet experiment is kept constant at 10 MPa during the deformation. The experiment was performed at room temperature with a confining pressure of 20 MPa and a constant rate of 1.3×10^{-6} s^{-1}.

The rock sample is roughly in the shape of a cylinder with diameter 20 mm and length 40 mm. Two piezoelectric transducers are glued at two opposite sides of the rock sample, and are used as a source and a receiver, respectively. For the purpose of gluing the transducers, the two opposite sides of the sample are cut 0.6 mm off and polished, as shown in Figure 1a. The receiver transducer records the compressional waves and shear waves traveling perpendicularly to the compression direction. P-wave and S-wave are generated and recorded separately using piezoelectric transducers located at the symmetrical sides of the center point at the edge (Figure 1b). The P- and S-wave waveforms with increasing differential stress are plotted in figures 2 and 3. Each trace in the plot is a stacked signal under each compression condition during the rock deformation before the failure of the rock sample. When the compression stress approaches the critical state, which varies from one rock sample to another, the rock breaks. All the experiments details can be found in Zaima and Katayama (2018).

The trend of the velocity structure can be seen in Figures 2 and 3. V_P and V_S both first increase and then decrease as compressional stress increases. In the early stage, V_P and V_S increase slightly due to the closure of the preexisting cracks perpendicularly oriented to the direction of the principal stress. At the second stage, the elastic wave velocities decrease owing to the opening of the micro-cracks and the following energy dissipation. Wave attenuation effects can be clearly observed when the stress approaches a threshold or for the later arrived seismic signals.

2.2 Forward modeling of 3D elastic waves using spectral element method

We use the spectral-element code SEM3D (Delavaud, 2007; Cupillard et al., 2012) to compute synthetic seismograms traveling through the cylindrical rock samples.

Here we briefly review the spectral-element method but the readers are referred to Komatitsch and Vilotte (1998); Chaljub et al. (2007); Peter et al. (2011) for more details. The SEM is based upon a high-order piecewise polynomial approximation of the weak formulation of the wave equation. It combines the accuracy of the pseudospectral method with the flexibility of the finite-element method. In this method, the wavefield is represented in terms of high-degree Lagrange interpolants per elements, and integrals are computed based upon Gauss-Lobatto-Legendre quadrature. Combined with a tensorial formulation, it leads to a perfectly diagonal mass matrix, which in turn leads to a fully explicit time scheme that lends itself very well to numerical simulations on parallel computers. The is method allows a low dispersion error together with an accurate and implicit description of the boundary conditions. Nevertheless, the tensorial formulation imposes to use hexahedral meshes, which is often a difficulty. We model cut and glued rock samples mimicking laboratory conditions as close as possible.

The Galerkin weak form of equation of motion (Geller & Ohminato, 1994; Komatitsch & Vilotte, 1998) reads:

$$\left(\mathbf{T}\frac{\partial^2}{\partial t^2}+\mathbf{H}\right)\mathbf{u}(t)=\mathbf{g}(t), \tag{1}$$

where $\mathbf{T}$ is mass matrix, the stiffness matrix $\mathbf{H}$ relates the elasticity and anelasticity, $\mathbf{g}$ represents the source term, and $\mathbf{u}$ is the discretized displacement for each element/point in the model. We use the free surface boundary (natural boundary condition) for the whole medium. However, in the reality, the rock sample is surrounded by a silicone jacket with high attenuation and slow velocity that it could play a role as the pseudo-absorbing boundary with respect to the rock sample. In the study, we vary the anelastic properties of the jacket to match the observed waveforms in the first place, see the section 2.2.2.

In order to model anelastic attenuation in our time-marching spectral-element methods, SEM3D uses standard Zener linear solids (SLS) to approximate a nearly constant quality factor Q (Liu et al., 1976; Carcione et al., 1988; Moczo & Kristek, 2005; Emmerich & Korn, 1987). A Zener body consists of a spring in series of the medium properties in connection with their relaxed stage at time $t = \infty$. SLS assumes Q does not depend on frequency. In this study, we use 3 SLS on a band of relaxation frequency ranging from 33.3 kHz to 3.3 MHz that the configuration of Q^{-1} to the frequency when Q equals to 15 is shown as figure 5.

2.2.1 Meshing

The standard GLL quadrature of SEM requires hexahedral meshes. However, creating a nonstructured hexahedral mesh with acceptable computational cost and high accuracy for a complex geometry is challenging. In this study, we used Trelis (www.csimsoft.com) to mesh the model. The size of the element should be small enough for the highest frequency of ∼2.5 MHz. Furthermore, in the case of nonstructured meshes, we have to avoid creating too-distorted elements, which may produce unstable results for poor quality meshes.

In order to model wave propagation realistically with limited knowledge of the media and finite computational resources. We approximated the source and receiver transducers as points, and we seek by trial and error the boundary conditions. We thus propose to deploy silicone rubber surrounding the rock sample. Figure 8 shows the mesh used in our forward modeling. In order to avoid the numerical error caused by the contact between more than one medium, we must include a tripling layer as refinement at the boundaries of different material models as shown in Figure 8. The height of the cylinder is about two times larger than the diameter, being approximately 40 mm and 20 mm, respectively. Note that for a good accuracy, for a polynomial approximation of degree 5 per tensorial direction, it is necessary to limit the element size to no-more than one minimum wavelength per element. Considering the minimum S-wave velocity of 2500 m/s in the granite rock and the maximum target frequency of 2 MHz, the mesh size is set to be 0.3 mm in all models.

2.2.2 Boundary conditions

The rock samples used in laboratory experiments are roughly cylindrical rocks. However, the long-side cutting surfaces parallel on two sides form two sharp surfaces, thus forming an incomplete cylinder. These imperfection of the cylindrical nature can cause a non-negligible effect on the waveform. In addition, although the rock sample itself is the main target of our simulation, using only the simple single-material rock model has defects on modeling the waveform. Silicone rubber, glue, aluminum frame, shrink plastic attached to the granitic rock may effect the waves propagating in the rock. Therefore, we tend to add more nature physics to the model by steps, at the same time, balancing the accuracy of the model and the computation cost in order to find the suitable model setting. Therefore, we investigate the boundary conditions with extra physical layer to simulate the transducer waveforms. As shown in the figure 7 ab), the free-surface boundary rock model cannot reproduce the observations. First due to the rapid freely propagation of waves in the rock model and later due to the strong reflections caused by sharp faces at both ends of the cylinder. Hence, we attempt to modify the boundary conditions by surrounding the rock model with silicone rubber, as we performed the real experiments: a layer of glue and silicone rubber has to be attached to the rock sample on its cylindrical side to jacket the sample. This layer is used to isolate the oil from the rock sample and transducers. The physical parameters of this layer are calculated from the characteristics of silicone rubber used in the experiment, Shin-Etsu KE45W RTV silicone rubber (Table. 1). The layer is added to both the cylindrical and the side-cut cylindrical rock model. The differences of the waveforms between the cylindrical rock model, the rock model with only free-surface boundary and the rock model with surrounding silicone layer are compared in Figure 7. The additional low-velocity layer surrounding the cylindrical rock sample behaves as a modified boundary conditions to absorb some portion of wave energy, but still presenting some reflections. Between models (a) and (b) in figure 7, we can observe the subtle differences caused by the cut sides. Models (c) and (d) have similarity until 5.5 μs, which shows the first three peaks, after which the reflections from the antipodal point is larger than the real data with model (c). The cut sides on the model (d) provide additional reflection back to the inner rock model, thus the amplitude of its waveform decays faster and the phases of the waveform are not so regular as model (c). The comparison among the four models demonstrates that the more features reflecting the reality are used, the more similar the waveform to the real data. These results made the model (d) as our best model for this study.

Table 1. The description of physical parameter of Shin-Etsu KE45W RTV silicone rubber (*Properties: Silicone Rubber*, 2020)

Physical parameter	Value
Density	1050 kg/m^3
Bulk modulus	1.5-2 GPa
Poisson's ratio	0.47-0.49
Shear modulus	0.0003-0.02 GPa
Young's modulus	0.001-0.05 GPa

2.2.3 Source and transfer functions

In addition to the boundary setting and model geometry, the source and the source-receiver position will also cause a significant impact on the waveform. Based on the laboratory experiment description (Zaima & Katayama, 2018), two different sources are applied. P-wave source is sent by moment tensor of diagonal components propagating perpendicularly to the rock surface and S-wave source is sent by moment tensor of x-z off-diagonal components. The source time function $S(t)$ is formally taken from the experiment input waveform. However, the absolute amplitude of the input signal transmitted to the rock by the piezoelectric transducers is unknown. Therefore, in this study, we estimated the effective source time function by a trial-and-error approach. We conclude that the recorded input waveform low-pass filtered at 2 MHz is the best source time function to be used. This is the same dominant frequency band used in laboratory experiment (Figure 4).

During the experiments, compressional and shear waves are transmitted independently at different source positions and their strain waveforms are recorded at their corresponding antipodal points. In the reality, the transducers are glued to the rock sample. However, due to the unknown coupling between the transducers, silicone rubber, and the rock sample, we consider four possible effective source-receiver distributions: (i) both the source and the receiver are slightly shifted inside to the region of the rock model; (ii) both the source and the receiver are slightly shifted outside to the region of the surrounding model; (iii) the source is slightly shifted outside to the region of the surrounding model and the receiver is inside to the region of the rock model; and (iv) the receiver is slightly shifted outside to the region of the surrounding model and the source is inside to the region of the rock model (Figure 9). The comparison between the experimental data of $\Delta\sigma=0$ and the synthetics of the four different source-receiver configurations is shown in Figure 10. Setting (ii) is considered to be the best source-receiver configuration and is later be used as the preferred source-receiver configuration in the study. Setting (iii) and (iv) have similar phases in the waveform, however, compared to setting (ii), the relative amplitude of the phase of the simulated waveform does not match the data waveform. When the source and receiver are both located slightly outside the edge of rock model, the first 5 peaks, which is from 4 μs to 6.2 μs, have higher amplitude than the other configurations. The possible reasons that the source and receiver must be set slightly outside the rock model will be discussed in section 4.

2.3 Processing of observed and synthetic data

Since we would like to directly compare the observed and synthetic data in order to infer the structural changes during the deformation experiment, we prevent introducing transfer function between observed and synthetic waveforms as we previously implemented (e.g. Lai et al. (2019)). Since the transfer function introduced in the previous study was to compensate the unrealistic setting of numerical modeling (2D linearly elastic), it is not anymore necessary to introduce it to match synthetic and observed data after careful treatments of 3D geometry, attenuation, boundary condition (see section 2.2.3). We perform data analysis, extracting maximum information from the original waveforms. Here, we introduce our strategy of filter and weighting function used for data analysis.

According to the spectrogram analysis in figure 6 , the strongest energy of the experimental waveform is focus in the frequency band between 1.6 MHz and 3 MHz for P-wave records and in the frequency band between 1 MHz and 2.8 MHz for S-wave. Compared to the S-wave spectrogram with concentrated energy, the energy of the P-wave spectrogram has a relatively low-frequency energy regions after 7 μs in addition to the most concentrated high-frequency region at the beginning. In this study, however, we want to focus on the changes in the high-frequency part. Therefore, we apply a butterworth bandpass filter from 1.5 MHz to 3.5 MHz for P-wave and from 1 MHz to 3 MHz for S-wave, which include the target region. After applying the filter, Hann window is used as weighting equations employed onto the waveforms in order to emphasize the importance of the match of the first-arrival, which is at the middle of a window we designed for. The waveforms and the fitting results with filter and weighting equation are later compared with the ones with no weighting equation shown in figure 11. Such a strategy of applying a weighting function undoubtedly increases the accuracy of the velocity model matching, avoiding being misled by the higher peaks that follow.

2.4 Inverse problem

We use waveforms of differential stress $\Delta\sigma$:

$$\mathbf{d}^T(\Delta\sigma) = \left[\mathbf{d}_{PP}^T(\Delta\sigma) \;\; \mathbf{d}_{SS}^T(\Delta\sigma)\right] \tag{2}$$

where $\mathbf{d}_{PP}$ and $\mathbf{d}_{SS}$ are time series vectors of compressional and shear waveforms recorded at a transducer receiver with compressional and shear transducer sources located at the antipodal site (Figure 1). The superscript ^{T} denotes transpose. We then generate synthetic seismograms $\mathbf{u}(\mathbf{m})$ with the same geometrical and source configurations for a set of seismological structural parameters $\mathbf{m}$. We define a misfit function to minimize:

$$S(\mathbf{m}, \Delta\sigma) = \alpha\left[1 - \frac{\mathbf{d}^T(\Delta\sigma)\mathbf{u}(\mathbf{m})}{|\mathbf{d}(\Delta\sigma)||\mathbf{u}(\mathbf{m})|}\right] + \beta\,|\mathbf{d}(\Delta\sigma) - \mathbf{u}(\mathbf{m})| + \gamma\,|\mathbf{d}(\Delta\sigma) - \mathbf{u}(\mathbf{m})|^2 \tag{3}$$

with α, β, γ, the weighting factors for zero-lag cross-correlation, L1-norm and L2-norm, respectively. We vary them to investigate the robustness of the inversion results. The misfit function equation 3 has to be computed with different weighting coefficients. First, equation 3 is used to constrain main phase with a large α (we discuss the explicit values in the results section). Second, equation 3 with large β and γ is used to investigate the amplitude of the waveform, and to further define the change in Q.

Aji granite is fine-grained and nearly isotropic, thus we can assume a homogeneous medium with the wavelength of 2-3 mm. We use four globally invariant parameters to represent the model vector $\mathbf{m}^T = (V_P, V_S, Q_P, Q_S)$. The time-lapse change of these global parameters will be related to the microscopic short-wavelength structural changes such as crack generation and the anelastic attenuation can be an indicator of the 3D elastic heterogeneity and intrinsic attenuation.

Based on the *a priori* information on the Aji granite, we set V_P varying from 3700 m/s to 5800 m/s and Q_P from 60 to 200 for the P-wave. As for the S-wave, V_S varies from 2660 m/s to 3550 m/s and Q_S from 20 to 90.

Note that all the comparison is based on the waveform analysis for $\Delta\sigma = 0$, which is the preferred model for the initial state of the experiment. We are interested in relative evolution of the velocity and attenuation parameters to the initial status $\Delta\sigma$, which is $\delta\mathbf{m}$, instead of the absolute values of $\mathbf{m}$. Therefore, the error during the estimation of $\mathbf{m}$ for $\Delta\sigma = 0$ will also combined in the offset of the absolute velocity in the following differential stress $\Delta\sigma$. $\delta\mathbf{m}$ can thus give us the insight into the relative changes of the rock.

2.4.1 Choice of range of seismic parameters for Monte-Carlo inversions

After determining the preferred model for the initial state (Figure 8), we performed 6000 simulations of different velocity models and different attenuation models. Since the volume of the rock did not change much in the experiment, we did not consider the variation in the rock density caused by the deformation. We make a hypothesis that the apparent density, which is 2650 kg/m^3, does not changed during the process of deformation of rock samples, but the internal velocity structure does. We fix the elastic parameters and the attenuating parameters of the silicone rubber jacketing model and modify systematically the parameters of the rock model for the purpose of creating a large database including different possibilities as shown in the table. 2. In addition, we can roughly have the idea of the possible range of P- and S-wave velocity during the process of the compression deformation from the previous studies on Aji granite deformation (Watanabe & Higuchi, 2015; Zaima & Katayama, 2018) where V_P varies approximately from 5600 m/s to 3500 m/s and from 3400 m/s to 2700 m/s, respectively. Therefore, we first simulate the P-wave velocity from 4700 m/s to 5800 m/s with a step of 20 m/s. Then, from 3700 m/s to 4600 m/s with a step of 100 m/s. As for the S-wave velocity range of simulation, 2660 m/s to 3550 m/s with a step of 10 m/s.

For P-wave strain matching, not only V_P and Q_P should be considered during the test, but also the impact of the S-wave on the P-wave waveform. The compressional to shear wave velocity ratio (V_P/V_S) is an important parameter in seismic analysis. Tatham (1982) mentioned that crack, pore, and geometry has a stronger effect on observed V_P/V_S ratios than the elastic constants of the minerals. Wang et al. (2012a) measured V_P/V_S ratios of cracked Westerly granite that they found the ratios range from 1.6 to 1.8 in the dry case at high frequency condition. Zaima and Katayama (2018) indicated that V_P/V_S ratios are nearly constant from 1.5 to 1.7 in the first stage and later decrease with increasing stress in dry experiments in Aji granite as well. Based on the above considerations, in our first step of data processing, for P-wave waveform simulation, we change the elastic parameters of V_P, Q_P, and the V_P/V_S but set the Q_S constant. As for the V_S parameter inputs, they are calculated from the varying V_P/V_S from 1.5 to 1.7 with step equals to 0.05. For the S-wave waveform simulation, we thus change the elastic parameters of V_S, Q_S, and the V_P/V_S but set the Q_P constant. During data processing, we take the best model calculated from equation 3 and narrow down the range of parameters to approach to the best value. The new model with V_P, V_S, Q_P and Q_S are applied based on the best value and the narrower velocity steps, $\Delta V'$, and attenuation step, $\Delta Q'$. We use the best result obtained by the first numerical simulation as the center value, and expand it by one step toward positive and one negative, creating a small

Table 2. Setting range of elasticity parameters and attenuation parameters

Model	V_P (m/s)	V_S (m/s)	Density (kg/m^3)	Q_P	Q_S
rock	3700-5800	2660-3550	2650	10-200	10-90
silicone rubber jacketing	1390	138	1050	6	4
increment	5-100	5-20	-	5-20	5-10
				Total models:	6000

group of models similar to the previous best value. We perform waveform matching again so as to increase the accuracy of achieving the best match.

3 Results

3.1 Snapshot of the wavefield

Figure 12 shows some snapshots of the P-wave wavefield in our preferred model (figure 8) from 2 μs to 7 μs with time step of 1 μs. These snapshots are cross-section views of the sample at the same height as the source and receiver center. At t = 2 μs, the snapshot shows that the direct P-waves radiated from the source propagates toward the opposite side of the surface through the sample interior. No scattering or conversion at the sample surface occurrs at this time. However, because of the influence of the side-cut structure, the wave fronts are no longer spreading out in a regular concentric circle. The surrounding low-velocity layer outside sample causes a boundary condition that has similar effect to absorbing boundary condition but still retains the characteristics as a reflective surface. Therefore, in latter time steps, the reflection along the side is too weak to interference with the direct P-waves. Because our model is not a cylindrical model, the cut corners at the side of the source immediately create reflections. When the direct wave was reflected at the opposite side of the sample from the source (t = 4 μs), the reflected P phase (PP wave) formed and propagated back to the source side. Since the opposite side has two cut corner as well, two additional reflected waves also formed due to the geometry, which can be seen between 5 μs and 6 μs in wavefield snapshot (figure 12(d) and (e)) and in the waveform (figure. 7(d)). However, since the low-velocity silicone layer traps most of the energy of the direct waves, the reflection from the interface at the receiver side is not strong. The P-wave propagation snapshots at a later time (t = 7 μs) show a very complicated wavefield due to the overlap of different reflected and converted waves developed at the curved sample surface.

Figure 13 presents the snapshots of S-wave wavefield. The effects of side-cut geometry mentioned above can also be seen in S-wave snapshots. The S-wave arrives at the receiver at about 6 μs. The strongest amplitude is not the direct S-wave, but the waves coming subsequently along the interface between the two materials (figure 13(e)).

As the P- and S-wave propagate through the rock, a large-amplitude wave packet travels through the interface between the rock sample and the silicone jacketing layer. As time passes, another sort of large-amplitude wave packet traveling slowly along the curved surface of the sample is trapped due to the low-velocity characteristics of the peripheral layer. In general, once the wavefront reached the sharpe edges of the bottom and top of the cylinder, a strong reflection would occur and radiate to the model interior. However, the addition of silicone material slows down the propagation, this phenomenon does not affect the wavefield and waveform significantly in the time period we considered.

3.2 Velocity model evolution

Figure 14 shows the waveform fitting results on dry sample using different misfit functions: (a) zero-lag cross-correlation, (b) L1-norm and (c) L2-norm. In figure 14, we can observe the best solution to the waveform fitting through the 2D pattern. Among the three misfit functions, zero-lag cross-correlation can best match the velocity model with less deviation because it focuses on the matching degree of the phase. Compared with zero-lag cross-correlation, L1-norm and L2-norm both yield a poorer waveform matching under high compression stress conditions for detecting V_P and V_S. Therefore, the objective function has a larger weighting in the value of cross-correlation in latter velocity model determination. The P- and S-waveform fitting results on dry sample using objective function are shown as figure 15 and figure 16, respectively. Figure 17 shows the comparison of the best-fit V_P and V_S models of the dry sample and the hand-picking results from Zaima and Katayama (2018), indicating the evolution of the P- and S- velocity model. For the experiment under dry conditions, the general development trend of V_P and V_S are similar, and follows 3 stages: (1) Increasing stage: V increases as the $\Delta\sigma$ increases till $\Delta\sigma$ equals to ∼80 Mpa, (2) Transitioning stage: ΔV remain small when $\Delta\sigma$ is between 81-128 MPa, and (3) Decreasing stage: V drops rapidly after $\Delta\sigma$ exceeds a threshold. The highest P-wave velocity structure of dry experiment occurs when the difference between compression stress and confining pressure equals to 81-128 MPa. When it comes to the situation where the P-wave velocity of the medium reaches to the highest, the P-wave velocity rate variation stays relatively small as the pressure increases. After reaching the threshold that differential stress equals to 250 MPa, the velocity structure of the model drops abruptly, which we interpret it as the threshold of the dry rock. Compared to V_P, we can find the specific highest V_S when $\Delta\sigma$ equals to 105 MPa, which is right at the middle between 81-128 MPa. We can therefore consider 105 MPa as the turning point of the velocity model for the dry data. V_S increases in a small velocity rate until the differential stress reaching this turning point, then decrease in a small velocity rate as well until $\Delta\sigma$ reaches to 250 MPa, where the V_S drops suddenly. In dry experiment, the difference between the fastest and slowest compressional wave velocities is 940 m/s (∼18%). As for V_S, the difference is about 560 m/s (∼16%). The increase in velocity is larger for compressional waves (∼100 m/s) than for shear waves (∼40 m/s) (figure 17). The increase rate of the V_P is higher than V_S and the later decrease rate of V_P is also higher than V_S, too.

Similarly, the velocity evolution of wet sample follows the 3 stages (figure 18) of dry sample. In wet experiment, the difference between the maximum and the minimum V_P is 320 m/s (∼6.1%) and the V_S difference is about 425 m/s (∼13.7%). The increase in velocity is larger for compressional waves (∼40 m/s) than for shear waves (∼25 m/s).

However, the decrease rate of V_P is also smaller than V_S. Figure 19 shows that increasing compression stress has larger impact on P-wave velocity changes in dry data, on the contrary, has smaller effect on P-wave velocity changes in wet data. Compared to dry data, the difference between V_P and V_S evolution is larger in the wet data. The dV/V_0 of V_S of wet data decreases most when having the same stress stage. Furthermore, the turning point of velocity changes of wet data shows earlier than dry data. The increasing stage and transition stage of the wet data are much shorter than dry data.

In general, the velocity evolution obtained from numerical simulation is similar to the hand-picking results. However, in this study, the numerical simulated V_P is slightly lower for both dry and wet experiment and V_S is slightly higher than the results of Zaima and Katayama (2018) for dry and wet case when having low $\Delta\sigma$. Take dry experimental waveform matching for example, V_P variation trends of modeled and hand-picked results is similar. The results getting from two methods have larger difference when it comes to higher $\Delta\sigma$. V_S also has similar trend between numerical and hand-picked results, however, disagreement grows bigger when the differential stress arises. The reason of these difference may due to seismic dispersion induced by attenuation in viscoelastic media, which also appears to have more obvious impact on shear wave. Kjartansson (1979) modeled the relationship between velocity and the quality factor that the phase velocity increases with frequency and the 1/Q. Dispersion provides an explanation for the peaks coming earlier for the viscoelastic waveform rather than for the elastic waveform, which is the stronger the attenuation of the medium, the earlier the wave arrives. Based on our observation that the quality factor decreases with the increase of $\Delta\sigma$, we suggest that the difference between the results of our waveform matching and previous study comes from our consideration of the attenuation factor and the stronger dispersion as the attenuation increase.

3.3 Attenuation parameters evolution

The variations of Q_P^{-1} and Q_S^{-1} along the increase of compression stress are compared in figure 20(a). For both dry or wet experiment, attenuation shows different varying behavior to velocity during the increase of effective stress. For dry experiment, Q_P varies initially from 250 to 10 and Q_S varies from 100 to 20 along the increase of differential stress. Unlike velocity change, Q_P^{-1} maintains the similar value steadily when $\Delta\sigma$ varies from 0 to 298.2 MPa. Only after $\Delta\sigma$ reaches 254 MPa does Q_P^{-1} start to rise gradually. While $\Delta\sigma$ exceeds 324 MPa, Q^{-1} grows rapidly. Q_S results show a silimar behavior. Yet $1/Q_S$ rises greatly when $\Delta\sigma$ exceeds 298.2 MPa, which is later than the P-wave. It shows that the internal structural changes of the rock have a greater impact on the attenuation of the P-wave in dry case. Note that the gradual change of Q_P is relatively obvious from 254 to 324 MPa, while Q_S has almost no gradual connection from low to high change rate. For the wet experiment, Q_P varies initially from 130 to 170, and from 170 to 20. Q_S varies from 80 to 110, and from 110 to 20 along the increase of differential stress. The evolution trends of Q_P and Q_S of the wet experiment are similar. This may be because of the fact that the wet experiment did not apply the same high pressure as the dry experiment because the water-saturated sample breaks earlier than the dry one. Another difference is that Q evolution obtained from wet data, the attenuation decreases first and then increases, corresponding to the evolution of the velocity and cannot to be easily observed in dry data.

Since we do not know the absolute amplitude of the wavelet input and the conversion formula of the transducer, we do not discuss the absolute value of Q but the relative change of Q. Figure 20(b) compares the Q^{-1} variation between different experiment and shows the relative change of Q^{-1}/Q_0^{-1}. The relative change of Q^{-1}/Q_0^{-1} shows that the attenuation of saturated rock is stronger than the dry rock regardless the type of wave. In dry rock, $Q_P < Q_S$ during the compression. On the contrary, $Q_P > Q_S$ during the compression in water-saturated rock. Under the same compressional pressure, attenuation of wet sample is higher than dry sample and the wet sample is more sensitive to the attenuation variation.

3.4 Waveform fitting

Waveform measurements were made during the increase in compressional pressure. Figures 21 and 22 compares the P- and S-wave strain waveforms obtained from the dry laboratory experiment (figures 2 and 3) and the best-fit numerical simulation results after performing three waveform matching steps, which is used for narrowing the target range. In addition, figures 23 and 24 compares the P- and S-wave strain synthetic and experimental waveforms obtained from the wet experiment.

By observing the best matching waveform under each pressure condition, it can be found that the first-arrival of both the P- and S-wave waveform gradually increase and decrease as the compressional pressure increases. In figures 21 and 23, the first three peaks of the synthetic P-strain waveforms can all fit well with the experimental data. After 6 μs of figure 21 and 6.8 μs of figure 23 where the fifth peak or sixth peak should expose, respectively, the shear waves come in that the waveforms do not fit well with the data because of the interference between the P- and S-wave energy. When $\Delta\sigma$ goes to 349.23 MPa of dry data set, the previously disappearing fifth peak reappeared in figure 21, which may due to the shear wave first arrival happens to be a constructive interference with the P-wave waveform. In the laboratory experiments, the S-wave may have little effect on the recorded P-wave strain waveform. When $\Delta\sigma$ exceeds 373.75 MPa for dry data, the interior structure of the rock is discontinuous and so different from the homogeneous model and cannot be modeled anymore. In figures 22 and 24, synthetic S-strain waveforms match well with the first two peaks experimental waveforms. However, after the third peak, the waveforms do not follow the experimental data. After the third peak, the waveforms of the experimental data have more peaks coming and having smaller amplitudes. Same as P-wave strain, when $\Delta\sigma$ exceeds 373.75 MPa for dry data, the interior structure of the rock is fragmentary and so different from the homogeneous model that cannot be modeled anymore. Compared to P-strain wavefroms, S-strain simulated waveforms are more difficult to match with the data. The difficulty may come from our homogeneous model assumption that has a greater impact on S-wave scattering and attenuation. Another possible reason is that the experimental data may not only record the SH-wave strain but also other waves. The third possibility is that our boundary condition is still deficient, causing the S-wave to have poor matching. However, matching the first few peaks has been able to provide enough information on the velocity model and attenuation parameters change.

4 Discussion and conclusions

4.1 Effect of the 3D model settings and geometry

We obtain the variation of velocities and attenuation from waveform matching and since the waveform is highly dependent on model geometry and especially, boundary condition, effect of the model geometry has to be carefully taken care of. Meanwhile, according to Burgos et al. (2016), the energy of the source is strongly related to the elastic properties at the point source. In order to approximate the experimental conditions, four source-receiver positions (figure 9 and 10) and four models with different boundary properties are tested (figure 7).

The results of the numerical experiments are comparable to the experiments by Yoshimitsu et al. (2016), although they performed the experiment on stationary aluminum sample rather than granite being deformed. In addition, they used lasers as a source and receiver rather than transducers. Yoshimitsu et al. (2016) modeled waveforms and matched their experimental data in order to analyze geometric effect on the wavefield. They implemented numerical modeling on a 3D cylindrical model and filtered the waveforms using two band-pass filters of 200–400 kHz and 400-800 kHz, which are lower than our filter band. They observed the body and surface wave propagation being influenced by the cylindrical geometry. In our numerical model (figure 7(a) and (b)), we observe the same phenomenon of large-amplitude surface waves emerged along the curved surface of the sample after the body waves. Furthermore, vertically propagating surface waves were generated after the body wave conversion at the corner, dominating the waveforms in the later coda of the records. However, in our experimental data, these large-amplitude surface waves are not be observed. Yoshimitsu et al. (2016) added absorbing boundary conditions; we introduce an additional layer with physical properties of silicone surrounding the target rock model, which is closer to the actual experimental situation (figure 8). Simultaneously, the accurate rock geometry must be carefully considered because we found that the two cuts parallel to compressional pressure are indispensable. The two cuts are the grinding cuts necessary to fix the transducers. They produce many extra reflections that the simple cylindrical model did not have and therefore further diverting some energy from the direct waves. From the results of numerical experiments (figure 7), these subtle geometries of model remarkably affect the results. Therefore, the accuracy of the three-dimensional geometry of the main rock model cannot be ignored.

The surrounding silicone rubber layer can provide a buffer-like region, which can slow down and reduce surface waves propagating between the two media. Note that when the direct waves reach the interface between the two materials and travel through a low-Q and low-velocity material, the resulting wavefield is amplified. Figure 25 shows the transmission coefficient T_{PP} and T_{SS} (Lay & Wallace, 1995), calculated as amplitude and phase at the solid-solid interface from rock to the silicone rubber model. When the incidence angle equals to 0, T_{PP} can be higher than 1.75, which can prove our observation that the amplification happens to the direct P-waves when they transmit the boundary. Therefore, the amplification and the buffer enhance the difference between the single-material rock model and the model with silicone rubber layer (model (b) and (d) in figure 7).

4.2 Changes in wave velocity and attenuation during deformation

Velocity and attenuation evolution of laboratory experiments under a physical state can provide a view of the underlying general mechanism during compression and transient waves propagating in the media. The simultaneous modeling of four elastic and viscoelatic parameters, V_P, V_S, Q_P and Q_S, provide a more accurate velocity and attenuation structure evolution. Since these four parameters affect each other and influence resulting waveforms, it becomes extremely important to balance their model space. However, by varying four possible parameters at the same time with all possibilities, we do not need to consider this problem.

In general, the variation of wave velocity (figures 17 and 18) during deformation estimated from waveform matching has a similar trend as seen by Zaima and Katayama (2018). The modeled velocity results compared to the experimental results are slightly lower (P-wave) or higher (S-wave) similarly. However, as the compression stress increases, this regularity gap will no longer be constant, but will have a larger gap. This phenomenon can be seen especially in the S-wave velocity of the high-stress stage. In the experiments, travel times were determined by a double picking technique in which the first arrival was estimated from the first peak minus a quarter period. This technique has a relatively large uncertainty particularly for highly dispersed sample approached failure, which may explain the difference between hand-pick and modeling velocity. Figure 19 can better give us an idea of the velocity changes at each stress stage. In dry data, P-waves are more sensitive to the growing stress. Otherwise, S-waves are more sensitive in wet data. Both V_P and V_S of wet data reache the highest point quicker than the results of dry experiments. The V_S of wet data, decreases to its lowest point the fastest.

To calculate Q_P and Q_S variations, Toksöz et al. (1979) studied the spectral ratios of waveform records of rock experiment relative to the waveform of reference sample. Lockner et al. (1977) and Zaima and Katayama (2018) used the amplitude ratios, which is taken from the differences between the first and second peaks of each phase arrival, to estimate the attenuation for increasing pressure. Moreover, S. A. Stanchits et al. (2003) calculated P-wave attenuation from relative amplitude loss. However, using the method proposed in this study, attenuation is no longer needed to be measured through waveform amplitude but by waveform modeling and auto-matching. Including Q_P and Q_S, in the simultaneous simulation increase the matching accuracy of the misfit functions, especially for L1-norm and L2-norm. In particular, synthetic waveforms ignoring Q_P and Q_S are not comparable to the highly compressed experimental data. In addition to the change of phases and amplitude, the travel time also can be changed by Q_P and Q_S (Kjartansson, 1979). The effect of attenuation on the velocity model determination can be observed in the comparison of the travel time between the hand-picked results and the velocity model obtained by our S-waveform matching for both dry and wet experiments (figure 17 and 18). The trend of V_S evolution calculated from hand-picked travel time is no longer consistent with synthetics, when differential stress exceeds 250 MPa and 200 MPa in dry and wet data, respectively. Apart than error caused by the picking technique, not considering the effect of the attenuation coefficient may also lead to differences. Therefore, the hand-picked velocity is always higher than our results when strong attenuation exists.

Since Zaima and Katayama (2018) implemented relative amplitude changes to quantify the attenuation condition, it is hard to compare our results of attenuation variation history. Nevertheless, the amplitude of the S-wave is reduced more than that of the P-wave during deformation under saturated wet conditions, which is consistent with our results (figure 20). Moreover, our inverse method with numerical simulation can directly consider the attenuation coefficient and the the velocity at the same time, and provide better results. Either P-wave or S-wave attenuation coefficient evolution of wet data is roughly opposite to the velocity evolution trend. The velocity increases while attenuation declines, and the attenuation grows while velocity declines. By comparing figure 19 and figure 20, we can see that attenuation coefficients change patterns and velocity change characteristics have strong similarities.

4.3 Inverse problem and waveform modeled in homogeneous media

The proposed method in this paper can process large amounts of experimental data quickly and provide the best matching value of V_P, V_S, Q_P, and Q_S. However, the method does not work well when longer lapse times are analyzed. For example, the fifth peak of the synthetic waveforms in figure 21 cannot match the data. Besides, the time when the fifth peak appears, it is also the arrival time of S-wave. Therefore, we conducted a numerical simulation experiment that set the S-wave velocity to a smaller value, which lets the S-wave train arriving after 8 μs (figure 7(d)). In this case, the fifth peak of the obtained waveform can match with the data. Therefore, we suppose this is because the data waveform has no ability to record SV-wave that causes the unmatched difference.

Full waveform inverse problem must inevitably move towards the development of heterogeneous models. So far we can only match the first few peaks in the waveform to get the elastic and viscoelastic parameters. But if we want to get more information on the weakening of rock materials from the waveform, we must use a more complex model. Only through heterogeneous model or even anisotropic model we could better simulate the structural changes and mechanisms inside the rock during deformation.

4.4 From the numerical simulation to crack development

Experimental studies found seismic wave attenuation in dry rocks sensitive to strain (Gordon & Davis, 1968; Tisato & Quintal, 2014). The mechanisms responsible for such loss of energy can be related to intrinsic material anelasticity, thermoelastic effects, friction at grain boundaries and micro-cracks developement (Simmons & Brace, 1965; Walsh, 1965; Johnston et al., 1979; Winkler & Nur, 1982; Guéguen & Schubnel, 2003). As for saturated rocks, the end-member consensus is that in addition to the above factors, energy is also dissipated as a consequence of fluid-related mechanisms. Winkler and Nur (1982) even declared that the effect of frictional sliding to the attenuation is negligible when it comes to rocks with pore fluid. They hence emphasized the importance of the role of intercrack fluid flow, which may consider as the major cause of the attenuation. In their experiments of dry, partially saturated, and saturated rock, they declared that S-wave attenuation increases with the degree of saturation and reaches its maximum at total saturation. However, as saturation continues to increase to more than 90 percent water saturation, Q_P is higher than during partial saturation condition and $Q_P > Q_S$. These observations can be explained with local fluid flow mechanisms. Guéguen and Schubnel (2003) also referred to the importance of local fluid flow and squirt flow on the characteristics of acoustic waves passing through rocks, but mainly on their influence on dispersion and anisotropy. They introduced models that numerically obtain dispersion for two different transversely isotropic distribution of cracks. For the model with a distribution of horizontally aligned cracks, the dispersion on P-wave and SV wave is small in the horizontal plane of the rock. However, SH wave shows no dispersion. For the model with a distribution of vertical cracks shows that the dispersion on P-wave and on SH wave is maximum in the horizontal plane, where SH wave has slightly higher dispersion than the P-wave.

Figure 19 compare the velocity evolution of dry and saturated wet experiment. The velocity results show that the presence of saturated water accelerates the state where the rock reaches its maximum velocity, which is the state closest to the non-crack mode. The presence of water also causes the fast reduction shear waves. Figure 20 plots the waveform fitting results of dry and fully-saturated wet experiment together, showing that attenuation changes along the increasing compression stress under different water conditions. The velocity results indicate that fully-saturated S-wave has greater decrease than P-wave, and the attenuation results suggest that the fully-saturated S-wave has greater attenuation than P-wave from low pressure until the rupture. These changes in elastic characteristics are consistent with the observation of Winkler and Nur (1982), which may be the same as the effects caused by intercrack flow. At the beginning, increasing of pressure causes little effect on both the P- and S-wave attenuation of dry and wet samples, because there is no enough density of cracks that affect the wave propagation. As the effective stress increases, our results show that $Q_S < Q_P$ in the wet case, on the contrary, $Q_P < Q_S$ for the dry case. This may be produced that when there is a high enough compressional pressure to form micro-cracks with higher density, especially with micro-cracks aligned vertically to the long axis. These highly dispersed waves lead to a large amount of attenuation. The characteristics and the local pore fluid flow (Winkler & Nur, 1982; Guéguen & Schubnel, 2003) can explain the feature of our attenuation results obtained from fully-saturated sample.

At low confining pressure, the micro-cracks in the experimental sample can be regarded as randomly distributed. The second stage is the closing process of horizontal micro-cracks, which are perpendicular to the maximum stress, leading to velocity increase. But, because the closure of horizontal micro-cracks has little effect on the energy dissipation of P- and S-wave, it is difficult to see the difference during the attenuation process.

Attenuation changes obtained from dry sample cannot be explained using the above interpretation since the saturated-wet and dry rock are dominated by different physical characteristics. The contribution to attenuation in the dry rock is assumed to be from the friction and the intrinsic aggregate attenuation only. Intrinsic attenuation is thought to be caused by energy dissipation because of friction at cracks where those faces are barely touching, making amplitude changes sensitive to crack geometry in the specimen (Lockner et al., 1977; Walsh, 1966). Besides, Bonner (1974) presented an increase of shear wave anisotropy in dry granite, which is caused by cracks oriented parallel or oblique to the compressional stress. This means that the cracks oriented parallel and subparallel to the axis of maximum compressional have influence on attenuation. However, we can see that many laboratory experiments confirmed that $Q_P < Q_S$ exists in the dried samples (Johnston et al., 1979), however, no specific mechanism has been proposed to explain the difference between P- and S-wave attenuation in dry rock.

Figure 26 compares the exact and relative V_P/V_S ratio obtained from waveform matching with the V_P/V_S ratio of Zaima and Katayama (2018). Christensen (1984); Audet et al. (2009); Peacock et al. (2011); Wang et al. (2012b) have mentioned that apparent V_P/V_S ratio rise can be found in the seismic data of the subduction zone or laboratory experimental data, which may be linked to the high pore fluid pressure and crack anisotropy when approaching failure. The V_P/V_S ratio obtained in this study satisfies the description of previous research. It is worth noting that there is a difference between the velocity variation curve we corrected through attenuation and the apparent $\mathrm{V_P/V_S}$ ratio (figure 26(b)). Our results present higher V_P/V_S ratios for wet experiment when rock approaches rock failure. Even in dry rock experiment, V_P/V_S ratios rise compared to the apparent V_P/V_S ratios when it comes to rupture. These may cause by the sudden rise S-wave anisotropy (Bonner, 1974) and thus influencing the attenuation and wave velocity. This characteristic of V_P/V_S ratio change marks the particularity of the rock right before failure, and may provide robust information on fracture prediction.

Through the matching of the simulated waveform and data, the velocity and attenuation changes can be obtained as the pressure rises up to rupture. Unlike previous studies, the determination of the amount of attenuation no longer requires amplitude analysis, but can be directly added to the numerical simulation and determined by full waveform matching. Under the condition of simultaneous changing velocity and attenuation coefficient for modeling, the waveform is no longer controlled by a single variable. Therefore, it can fix the velocity change caused by neglecting the attenuation coefficient when determining the change of the velocity model. Combining seismic simulation, waveform matching and rock experiment, the data measured can explain the fracture nucleation during varying stress conditions. We expect seismic methods to bring more useful information on small-scale rock fractures. Attenuation, velocity, and V_P/V_S ratio variation revealed in this study shows different trends from the usual rock measurements, so it may give us the opportunity to more effectively understand rock failure mechanism of not only laboratory experiments, but also the shallower part of the earth's crust.

Acknowledgments

This research is part of the PhD thesis of Ssu-Ting Lai, which is co-funded by French. National Program MOPGA (Make Our Planet Great Again) and Université de Paris, Institut de physique du globe de Paris. Numerical computations were partly performed on the S-CAPAD platform, IPGP, France. All the data are available through Zaima and Katayama 2018.

References

Audet, P., Bostock, M. G., Christensen, N. I., & Peacock, S. M. (2009). Seismic evidence for overpressured subducted oceanic crust and megathrust fault sealing. *Nature*, *457*(7225), 76–78. Retrieved from `https://doi.org/10.1038/nature07650` doi: 10.1038/nature07650

Benson, P., Schubnel, A., Vinciguerra, S., Trovato, C., Meredith, P., & Young, R. P. (2006). Modeling the permeability evolution of microcracked rocks from elastic wave velocity inversion at elevated isostatic pressure. *Journal of Geophysical Research: Solid Earth*, *111*(B4). Retrieved from `https://agupubs.onlinelibrary.wiley.com/doi/abs/10.1029/2005JB003710` doi: 10.1029/2005JB003710

Bonner, B. P. (1974). Shear wave birefringence in dilating granite. *Geophysical Research Letters*, *1*(5), 217–220. Retrieved from `https://agupubs.onlinelibrary.wiley.com/doi/abs/10.1029/GL001i005p00217` doi: 10.1029/GL001i005p00217

Brantut, N. (2018). Time-resolved tomography using acoustic emissions in the laboratory, and application to sandstone compaction. *Geophysical Journal International*, *213*(3), 2177–2192. Retrieved from `http://dx.doi.org/10.1093/gji/ggy068` doi: 10.1093/gji/ggy068

Burgos, G., Capdeville, Y., & Guillot, L. (2016). Homogenized moment tensor and the effect of near-field heterogeneities on nonisotropic radiation in nuclear explosion. *Journal of Geophysical Research: Solid Earth*, *121*(6), 4366–4389. Retrieved from `https://agupubs.onlinelibrary.wiley.com/doi/abs/10.1002/2015JB012744` doi: 10.1002/2015JB012744

Capdeville, Y., Vilotte, J. P., & Montagner, J. P. (2003). Coupling the spectral element method with a modal solution for elastic wave propagation in global earth models. *Geophysical Journal International*, *152*(1), 34–67. Retrieved from `https://onlinelibrary.wiley.com/doi/abs/10.1046/j.1365-246X.2003.01808.x` doi: 10.1046/j.1365-246X.2003.01808.x

Carcione, J. M., Kosloff, D., & Kosloff, R. (1988). Wave propagation simulation in a linear viscoacoustic medium. *Geophysical Journal*, *93*(2), 393–401. Retrieved from `https://onlinelibrary.wiley.com/doi/abs/10.1111/j.1365-246X.1988.tb02010.x` doi: 10.1111/j.1365-246X.1988.tb02010.x

Chaljub, E., Komatitsch, D., Vilotte, J.-P., Capdeville, Y., Valette, B., & Festa, G. (2007, dec). Spectral-element Analysis in Seismology. *Advances in Geophysics*, *48*, 365–419. doi: 10.1016/S0065-2697(06)48007-9

Chaljub, E., Maufroy, E., Moczo, P., Kristek, J., Hollender, F., Bard, P.-Y., ... Chen, X. (2015, feb). 3-D numerical simulations of earthquake ground motion in sedimentary basins: Testing accuracy through stringent models. *Geophysical Journal International*, *201*, 90. doi: 10.1093/gji/ggu472

Christensen, N. I. (1984, nov). Pore pressure and oceanic crustal seismic structure. *Geophysical Journal International*, *79*(2), 411–423. Retrieved from `https://doi.org/10.1111/j.1365-246X.1984.tb02232.x` doi: 10.1111/j.1365-246X.1984.tb02232.x

Cupillard, P., Delavaud, E., Burgos, G., Festa, G., Vilotte, J.-P., Capdeville, Y., & Montagner, J.-P. (2012, jan). RegSEM: a versatile code based on the Spectral Element Method to compute seismic wave propagation at the regional scale. *Geophysical Journal International*, *188*, 1203–1220. doi: 10.1111/j.1365-246X.2011.05311.x

De Basabe, J., & Sen, M. (2014, nov). Geophysical Journal International A comparison of finite-difference and spectral-element methods for elastic wave propagation in media with a fluid-solid interface. *Geophysical Journal International*, *200*, 278–298. doi: 10.1093/gji/ggu389

Delavaud, É. (2007). Simulation numérique de la propagation d'ondes en milieu géologique complexe : application à l'évaluation de la réponse sismique du bassin de caracas (venezuela)..

Di Carli, S., François-Holden, C., Peyrat, S., & Madariaga, R. (2010). Dynamic inversion of the 2000 Tottori earthquake based on elliptical subfault approximations. *Journal of Geophysical Research: Solid Earth*, *115*(B12). Retrieved from `https://agupubs.onlinelibrary.wiley.com/doi/abs/10.1029/2009JB006358` doi: 10.1029/2009JB006358

Emmerich, H., & Korn, M. (1987). Incorporation of attenuation into time-domain computations of seismic wave fields. *GEOPHYSICS*, *52*(9), 1252–1264. Retrieved from `https://doi.org/10.1190/1.1442386` doi: 10.1190/1.1442386

Fliss, S., Bhat, H. S., Dmowska, R., & Rice, J. R. (2005). Fault branching and rupture directivity. *Journal of Geophysical Research: Solid Earth*, *110*(B6). Retrieved from `https://agupubs.onlinelibrary.wiley.com/doi/abs/10.1029/2004JB003368` doi: 10.1029/2004JB003368

Gabriel, A.-A., Ampuero, J.-P., Dalguer, L. A., & Mai, P. M. (2012). The transition of dynamic rupture styles in elastic media under velocity-weakening friction. *Journal of Geophysical Research: Solid Earth*, *117*(B9). Retrieved from `https://agupubs.onlinelibrary.wiley.com/doi/abs/10.1029/2012JB009468` doi: 10.1029/2012JB009468

Geller, R. J., & Ohminato, T. (1994). Computation of synthetic seismograms and their partial derivatives for heterogeneous media with arbitrary natural boundary conditions using the Direct Solution Method. *Geophysical Journal International*, *116*(2), 421–446. Retrieved from `https://onlinelibrary.wiley.com/doi/abs/10.1111/j.1365-246X.1994.tb01807.x` doi: 10.1111/j.1365-246X.1994.tb01807.x

Gordon, R. B., & Davis, L. A. (1968). Velocity and attenuation of seismic waves in imperfectly elastic rock. *Journal of Geophysical Research (1896-1977)*, *73*(12), 3917–3935. Retrieved from `https://agupubs.onlinelibrary.wiley.com/doi/abs/10.1029/JB073i012p03917` doi: 10.1029/JB073i012p03917

Guéguen, Y., & Schubnel, A. (2003). Elastic wave velocities and permeability of cracked rocks. *Tectonophysics*, *370*(1), 163–176. Retrieved from `http://www.sciencedirect.com/science/article/pii/S0040195103001847` doi: https://doi.org/10.1016/S0040-1951(03)00184-7

Igel, H., Jahnke, G., & Ben-Zion, Y. (2002). Numerical Simulation of Fault Zone Guided Waves: Accuracy and 3-D Effects. In M. Matsu'ura, P. Mora, A. Donnellan, & X.-c. Yin (Eds.), *Earthquake processes: Physical modelling, numerical simulation and data analysis part i* (pp. 2067–2083). Basel: Birkhäuser Basel. Retrieved from `https://doi.org/10.1007/978-3-0348-8203-3{\_}11` doi: 10.1007/978-3-0348-8203-3_11

Johnston, D. H., Toksöz, M. N., & Timur, A. (1979). Attenuation of seismic waves in dry and saturated rocks: II. Mechanisms. *GEOPHYSICS*, *44*(4), 691–711. Retrieved from `https://doi.org/10.1190/1.1440970` doi: 10.1190/1.1440970

Kjartansson, E. (1979). Constant Q-wave propagation and attenuation. *Journal of Geophysical Research: Solid Earth*, *84*(B9), 4737–4748. Retrieved from `https://agupubs.onlinelibrary.wiley.com/doi/abs/10.1029/JB084iB09p04737` doi: 10.1029/JB084iB09p04737

Komatitsch, D., & Vilotte, J.-P. (1998). The Spectral Element method: an efficient

tool to simulate the seismic response of 2D and 3D geological structures. *Bulletin of the Seismological Society of America*, *88*, 368–392.
Kudo, Y., Sano, O., Murashige, N., Mizuta, Y., & Nakagawa, K. (1992). Stress-induced crack path in Aji granite under tensile stress. *pure and applied geophysics*, *138*(4), 641–656. Retrieved from `https://doi.org/10.1007/BF00876342` doi: 10.1007/BF00876342
Lai, S.-T., Fuji, N., & Katayama, I. (2019). Time-lapse elastic properties of cracked granite during deformation inferred from laboratory experiments using 2d waveform modelling. *The 81st EAGE conference and exhibition, London.*
Lay, T., & Wallace, T. (1995). Modern Global Seimology. In (Vol. 58).
Lee, S.-J., Huang, B.-S., Ando, M., Chiu, H.-C., & Wang, J.-H. (2011). Evidence of large scale repeating slip during the 2011 Tohoku-Oki earthquake. *Geophysical Research Letters*, *38*(19). Retrieved from `https://agupubs.onlinelibrary.wiley.com/doi/abs/10.1029/2011GL049580` doi: 10.1029/2011GL049580
Liu, H.-P., Anderson, D. L., & Kanamori, H. (1976, oct). Velocity dispersion due to anelasticity; implications for seismology and mantle composition. *Geophysical Journal International*, *47*(1), 41–58. Retrieved from `https://doi.org/10.1111/j.1365-246X.1976.tb01261.x` doi: 10.1111/j.1365-246X.1976.tb01261.x
Lockner, D. A., Walsh, J. B., & Byerlee, J. D. (1977). Changes in seismic velocity and attenuation during deformation of granite. *Journal of Geophysical Research (1896-1977)*, *82*(33), 5374–5378. Retrieved from `https://agupubs.onlinelibrary.wiley.com/doi/abs/10.1029/JB082i033p05374` doi: 10.1029/JB082i033p05374
Moczo, P., & Kristek, J. (2005). On the rheological models used for time-domain methods of seismic wave propagation. *Geophysical Research Letters*, *32*(1). Retrieved from `https://agupubs.onlinelibrary.wiley.com/doi/abs/10.1029/2004GL021598` doi: 10.1029/2004GL021598
Möllhoff, M., Bean, C. J., & Meredith, P. G. (2010). Rock fracture compliance derived from time delays of elastic waves. *Geophysical Prospecting*, *58*(6), 1111–1122. Retrieved from `https://onlinelibrary.wiley.com/doi/abs/10.1111/j.1365-2478.2010.00887.x` doi: 10.1111/j.1365-2478.2010.00887.x
Pageot, D., Leparoux, D., Le Feuvre, M., Durand, O., Côte, P., & Capdeville, Y. (2017). Improving the seismic small-scale modelling by comparison with numerical methods. *Geophysical Journal International*, *211*(1), 637–649. Retrieved from `https://doi.org/10.1093/gji/ggx309` doi: 10.1093/gji/ggx309
Paterson, M., & Wong, T.-f. (2005, jan). Experimental Rock Deformation - The Brittle Field. *Experimental Rock Deformation - The Brittle Field*, *348*. doi: 10.1007/b137431
Peacock, S., Christensen, N., Bostock, M., & Audet, P. (2011). High pore pressures and porosity at 35 km depth in the Cascadia subduction zone. *Geology*, *39*, 471–474. doi: 10.1130/G31649.1
Peter, D., Komatitsch, D., Luo, Y., Martin, R., Le Goff, N., Casarotti, E., ... Tromp, J. (2011). Forward and adjoint simulations of seismic wave propagation on fully unstructured hexahedral meshes. *Geophysical Journal International*, *186*(2), 721–739. Retrieved from `https://onlinelibrary.wiley.com/doi/abs/10.1111/j.1365-246X.2011.05044.x` doi: 10.1111/j.1365-246X.2011.05044.x
Properties: Silicone Rubber. (2020). `https://www.azom.com/properties.aspx?ArticleID=920`. (Retrieved 9 September 2020)
Scholz, C. H., Sykes, L. R., & Aggarwal, Y. P. (1973). Earthquake Prediction: A Physical Basis. *Science*, *181*(4102), 803–810. Retrieved from `https://science.sciencemag.org/content/181/4102/803` doi: 10.1126/science.181.4102.803

Scott, T. E., Ma, Q., & Roegiers, J.-C. (1993). Acoustic velocity changes during shear enhanced compaction of sandstone. *International Journal of Rock Mechanics and Mining Sciences & Geomechanics Abstracts*, *30*(7), 763–769. Retrieved from `http://www.sciencedirect.com/science/article/pii/014890629390020E` doi: https://doi.org/10.1016/0148-9062(93)90020-E

Simmons, G., & Brace, W. F. (1965). Comparison of static and dynamic measurements of compressibility of rocks. *Journal of Geophysical Research (1896-1977)*, *70*(22), 5649–5656. Retrieved from `https://agupubs.onlinelibrary.wiley.com/doi/abs/10.1029/JZ070i022p05649` doi: 10.1029/JZ070i022p05649

Solymosi, B., Favretto-Cristini, N., Monteiller, V., Komatitsch, D., Cristini, P., Arntsen, B., & Ursin, B. (2018). How to adapt numerical simulation of wave propagation and ultrasonic laboratory experiments to be comparable {\mdash} A case study for a complex topographic model. *Geophysics*, *83*, T195–T207. doi: 10.1190/geo2017-0536.1

Stanchits, S., Vinciguerra, S., & Dresen, G. (2006). Ultrasonic Velocities, Acoustic Emission Characteristics and Crack Damage of Basalt and Granite. *pure and applied geophysics*, *163*(5), 975–994. Retrieved from `https://doi.org/10.1007/s00024-006-0059-5` doi: 10.1007/s00024-006-0059-5

Stanchits, S. A., Lockner, D. A., & Ponomarev, A. V. (2003). Anisotropic Changes in P-Wave Velocity and Attenuation during Deformation and Fluid Infiltration of Granite. *Bulletin of the Seismological Society of America*, *93*(4), 1803–1822. Retrieved from `https://doi.org/10.1785/0120020101` doi: 10.1785/0120020101

Tatham, R. H. (1982). Vp/Vs and lithology. *GEOPHYSICS*, *47*(3), 336–344. Retrieved from `https://doi.org/10.1190/1.1441339` doi: 10.1190/1.1441339

Tisato, N., & Quintal, B. (2014). Laboratory measurements of seismic attenuation in sandstone: Strain versus fluid saturation effects. *GEOPHYSICS*, *79*(5), WB9–WB14. Retrieved from `https://doi.org/10.1190/geo2013-0419.1` doi: 10.1190/geo2013-0419.1

Toksöz, M. N., Johnston, D. H., & Timur, A. (1979). Attenuation of seismic waves in dry and saturated rocks: I. Laboratory measurements. *GEOPHYSICS*, *44*(4), 681–690. Retrieved from `https://doi.org/10.1190/1.1440969` doi: 10.1190/1.1440969

Walsh, J. B. (1965). The effect of cracks on the compressibility of rock. *Journal of Geophysical Research (1896-1977)*, *70*(2), 381–389. Retrieved from `https://agupubs.onlinelibrary.wiley.com/doi/abs/10.1029/JZ070i002p00381` doi: 10.1029/JZ070i002p00381

Walsh, J. B. (1966). Seismic wave attenuation in rock due to friction. *Journal of Geophysical Research (1896-1977)*, *71*(10), 2591–2599. Retrieved from `https://agupubs.onlinelibrary.wiley.com/doi/abs/10.1029/JZ071i010p02591` doi: 10.1029/JZ071i010p02591

Wang, X.-Q., Schubnel, A., Fortin, J., David, E. C., Guéguen, Y., & Ge, H.-K. (2012a). High Vp/Vs ratio: Saturated cracks or anisotropy effects? *Geophysical Research Letters*, *39*(11). Retrieved from `https://agupubs.onlinelibrary.wiley.com/doi/abs/10.1029/2012GL051742` doi: 10.1029/2012GL051742

Wang, X.-Q., Schubnel, A., Fortin, J., David, E. C., Guéguen, Y., & Ge, H.-K. (2012b). High Vp/Vs ratio: Saturated cracks or anisotropy effects? *Geophysical Research Letters*, *39*(11). Retrieved from `https://agupubs.onlinelibrary.wiley.com/doi/abs/10.1029/2012GL051742` doi: 10.1029/2012GL051742

Watanabe, T., & Higuchi, A. (2015, dec). Simultaneous measurements of elastic wave velocities and electrical conductivity in a brine-saturated granitic rock under confining pressures and their implication for interpretation of geophysical observations. *Progress in Earth and Planetary Science*, *2*. doi: 10.1186/s40645-015-0067-0

Winkler, K. W., & Nur, A. (1982). Seismic attenuation: Effects of pore fluids and frictional-sliding. *GEOPHYSICS*, *47*(1), 1–15. Retrieved from https://doi.org/10.1190/1.1441276 doi: 10.1190/1.1441276

Yoshimitsu, N., Furumura, T., & Maeda, T. (2016). Geometric effect on a laboratory-scale wavefield inferred from a three-dimensional numerical simulation. *Journal of Applied Geophysics*, *132*, 184–192. Retrieved from http://www.sciencedirect.com/science/article/pii/S0926985116301768 doi: https://doi.org/10.1016/j.jappgeo.2016.07.002

Zaima, K., & Katayama, I. (2018). Evolution of Elastic Wave Velocities and Amplitudes During Triaxial Deformation of Aji Granite Under Dry and Water-Saturated Conditions. *Journal of Geophysical Research: Solid Earth*, *123*(11), 9601–9614. Retrieved from https://agupubs.onlinelibrary.wiley.com/doi/abs/10.1029/2018JB016377 doi: 10.1029/2018JB016377

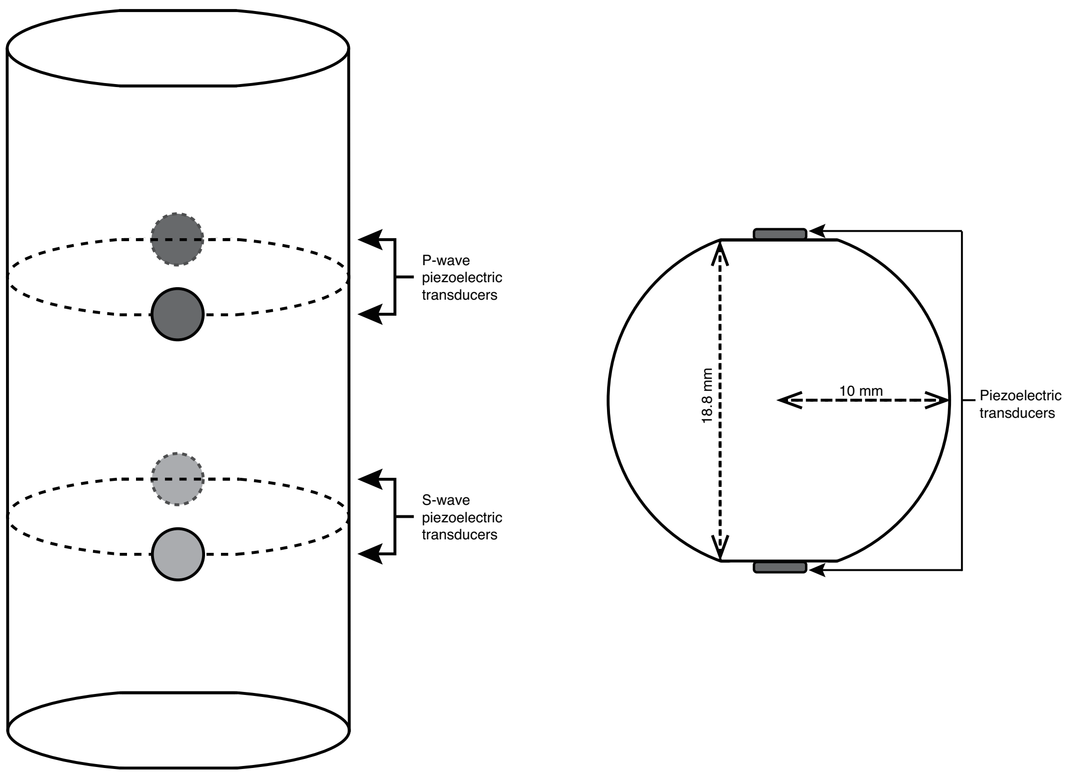

Figure 1. The schematic diagram of the geometry of sample and the position of the transducers. (A) The general view of the experimental setting of the sample. (B) The cross-section of the sample.

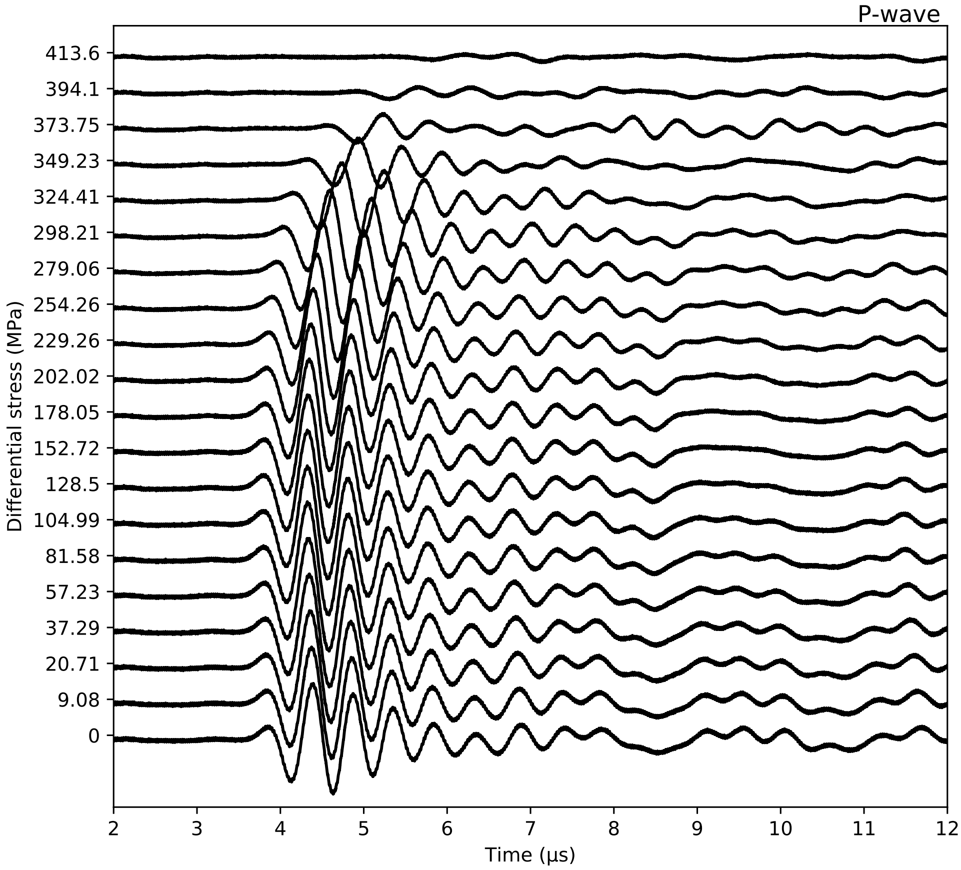

Figure 2. The P-wave experimental data recorded by transducer. The y-axis indicate the deformation progress and correspond to a condition of $\Delta\sigma$. The x-axis represents the time of wave propagation. (Courtesy of Zaima and Katayama (2018).)

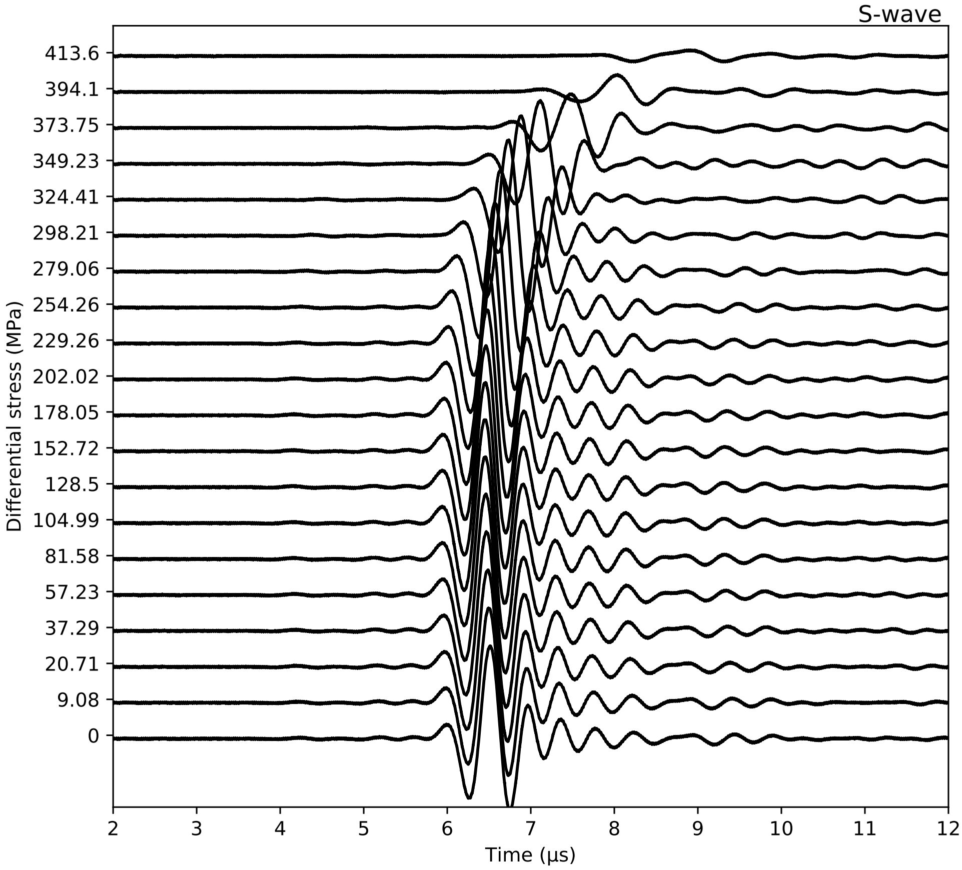

Figure 3. The S-wave experimental data recorded by transducer. The y-axis indicate the deformation progress and correspond to a condition of $\Delta\sigma$. The x-axis represents the time of wave propagation. (Courtesy of Zaima and Katayama (2018).)

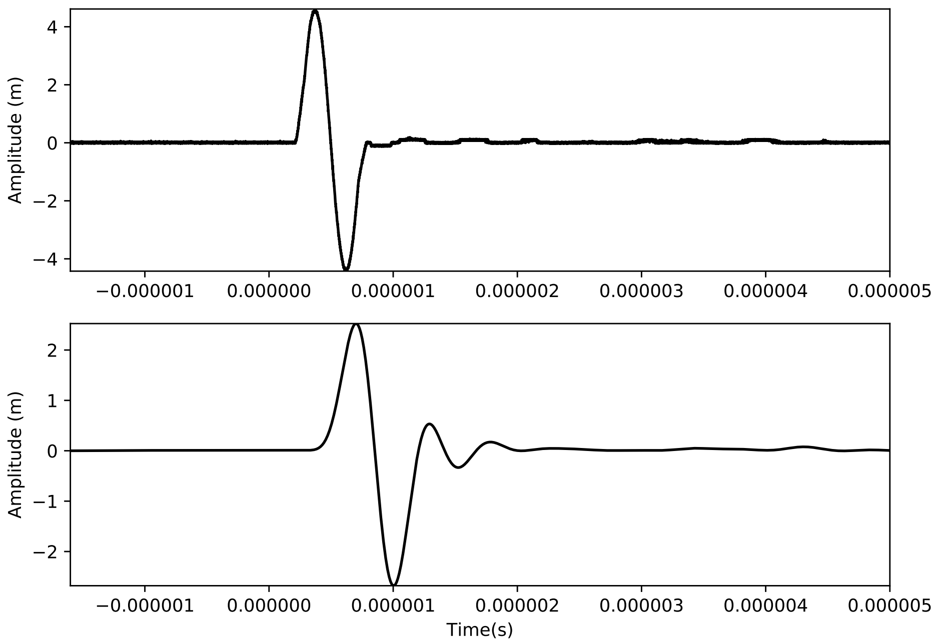

Figure 4. The input wavelet of the rock experiment (top) and the numerical modeling (bottom). In order to avoid the noise of the experimental wavelet, we use the filtered wavelet as the input.

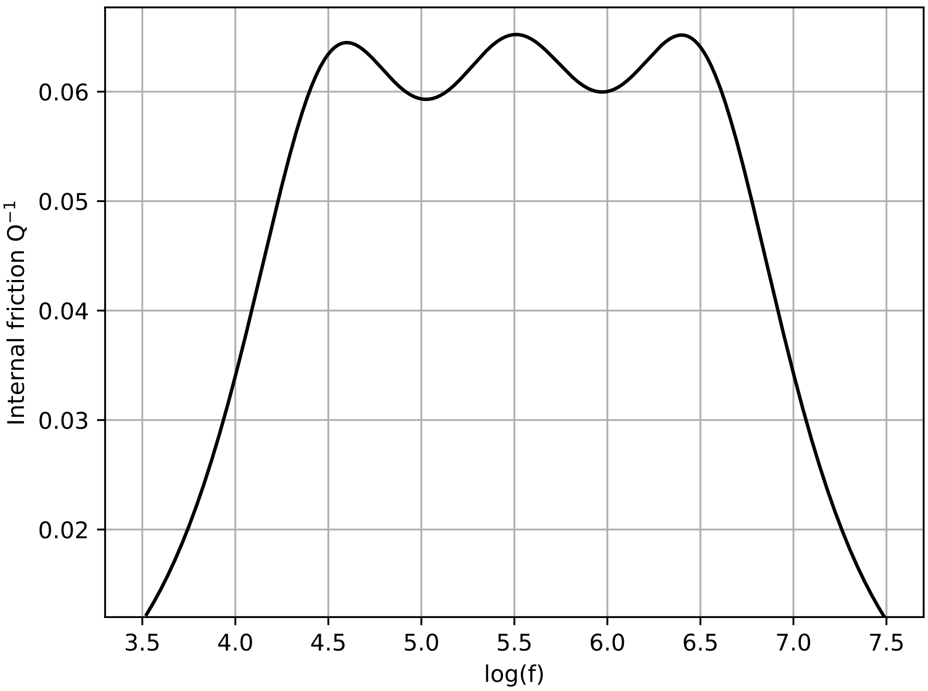

Figure 5. The internal friction plots Q^{-1}. Three SLSs are used for approximate the attenuation behavior.

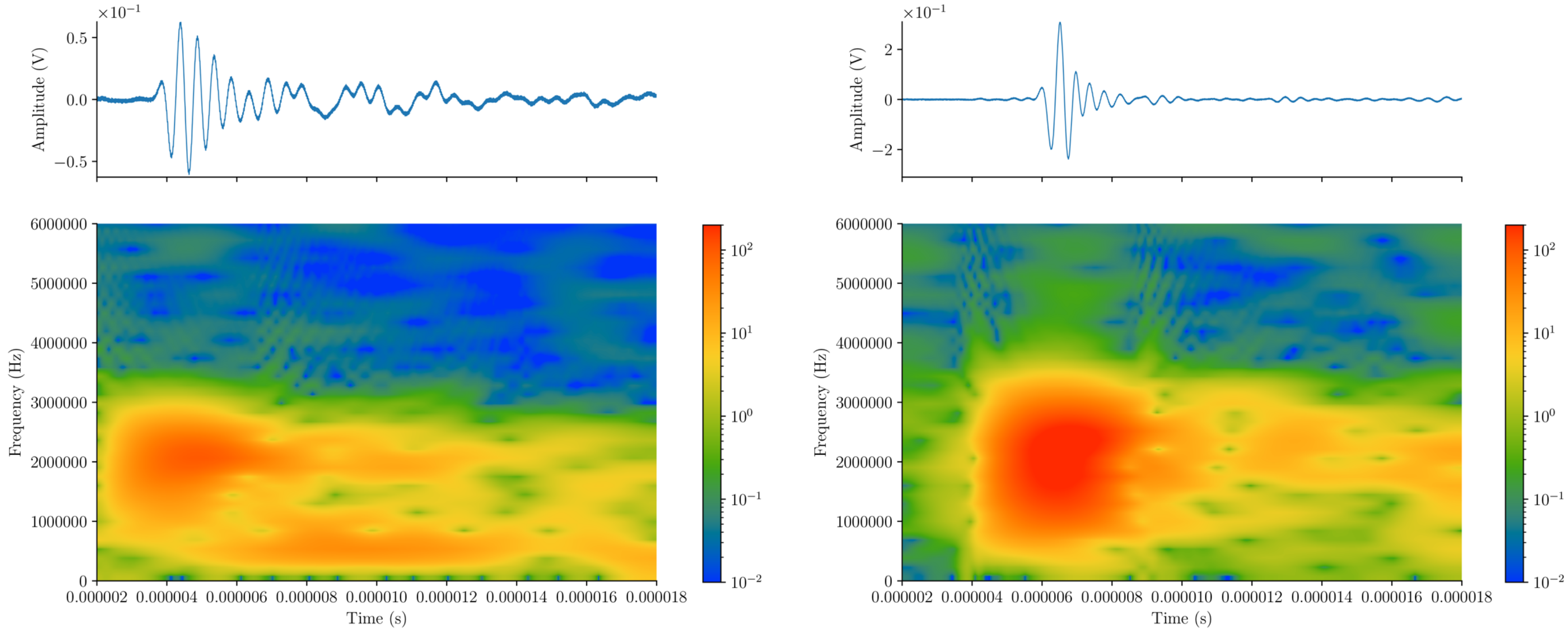

Figure 6. The (a) P- and (b) S-wave spectrogram of experimental data for 0 MPa differential stress.

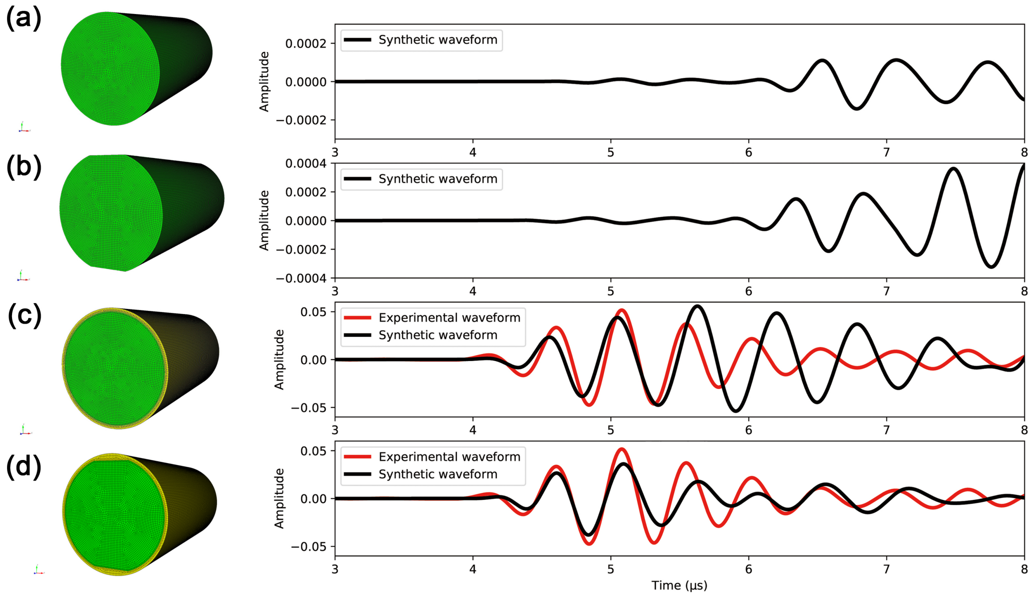

Figure 7. The four models tested in this study and their synthetic waveform (a) cylindrical model with free-boundary, (b) side-cut cylindrical model with free-boundary, (c) cylindrical model with surrounding silicone jacketing model and (d) side-cut cylindrical model with surrounding silicone jacketing model.

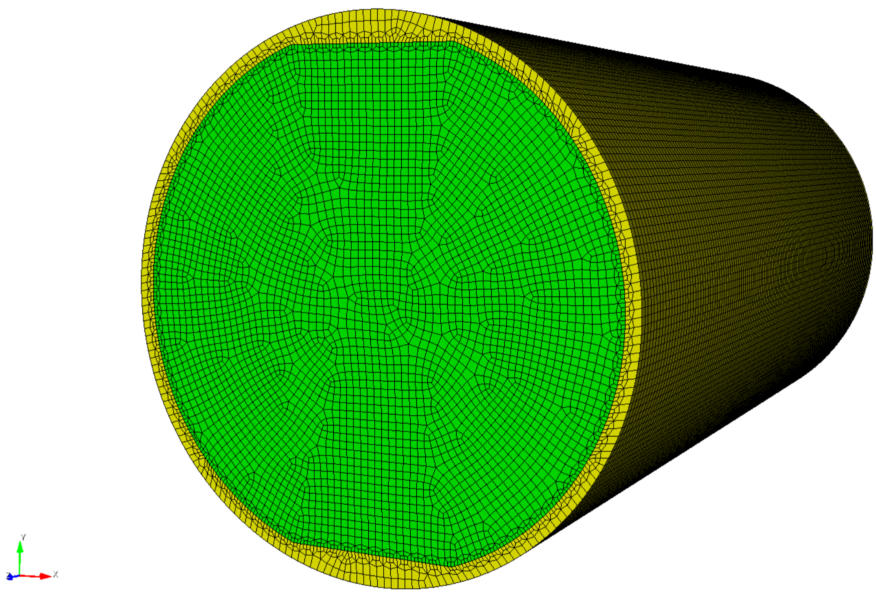

Figure 8. The distorted hexahedral mesh of the model for SEM. The green region is the rock model. The yellow part represents the surrounding low-velocity material. The mesh size is approximate to 0.3 mm.

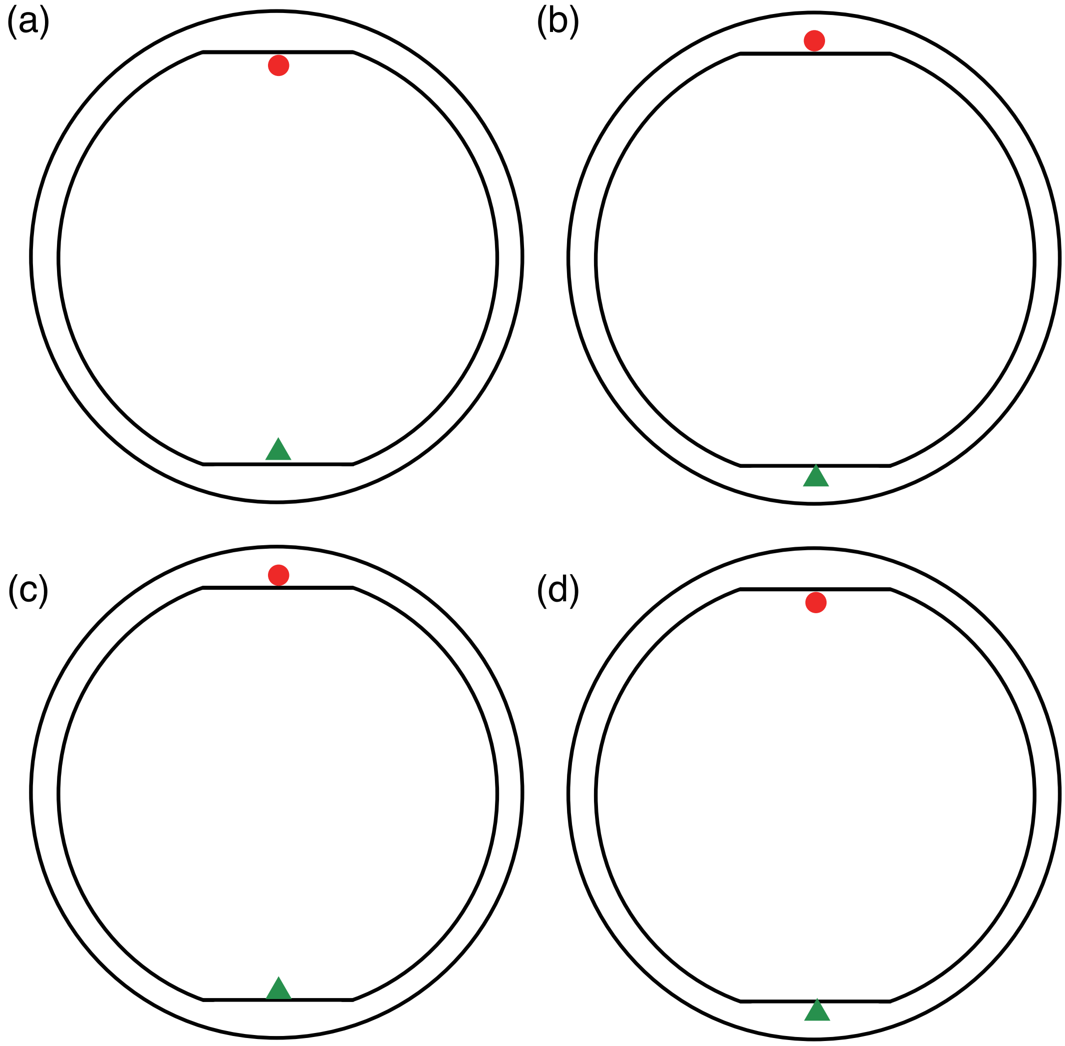

Figure 9. The four source-receiver positions tested in the study on the preferred model (figure 8). The red circle represents the source position; contrariwise, the green triangle indicates the receiver position. The (b) setting of the source-receiver position is determined to be the best.

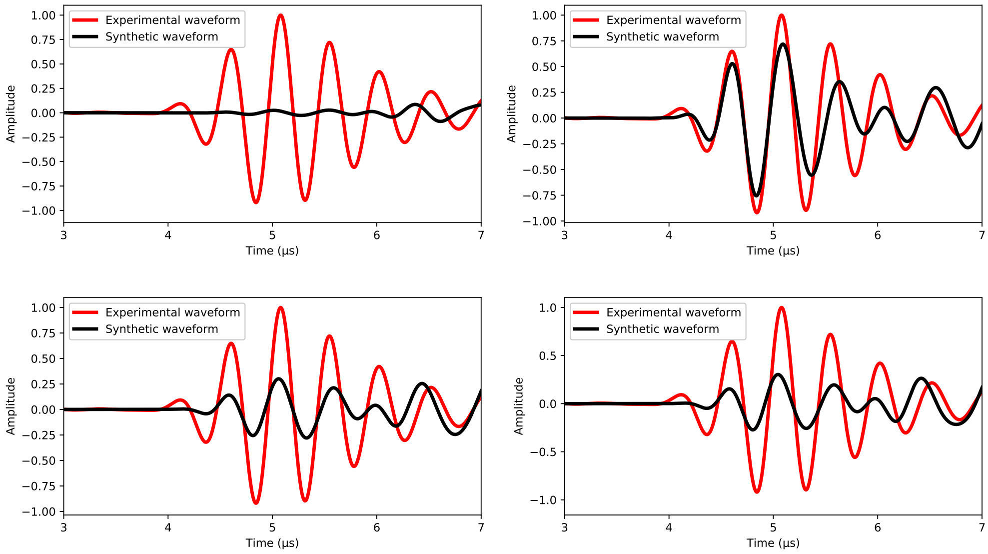

Figure 10. The four normalized-synthetic waveform compared to the data with different source-receiver positions according to figure 9.

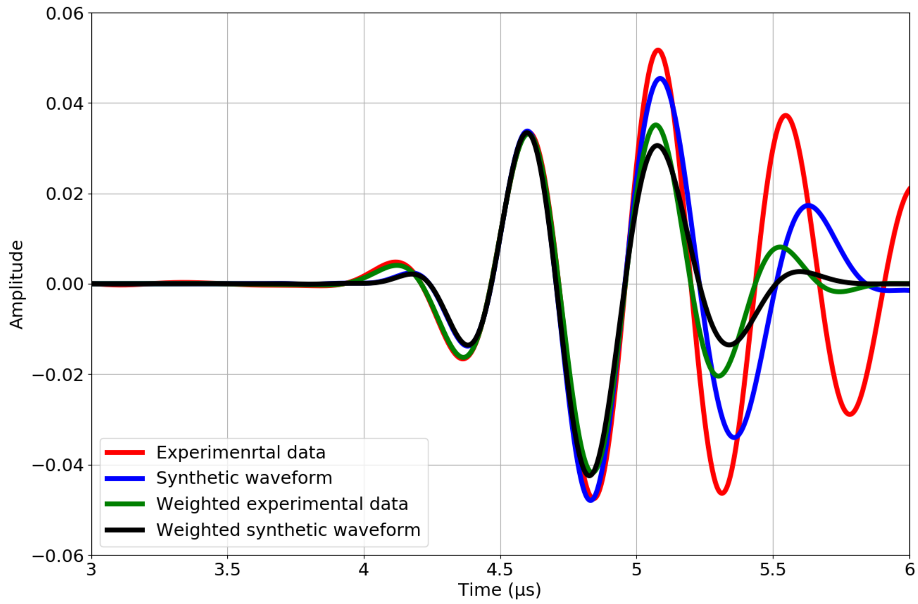

Figure 11. Waveform fitting using Hann window as weighting function from 3 to 6 μs. In order to emphasize the weight of first-arrival, the Hann window is applied on both the experimental and numerical waveform.

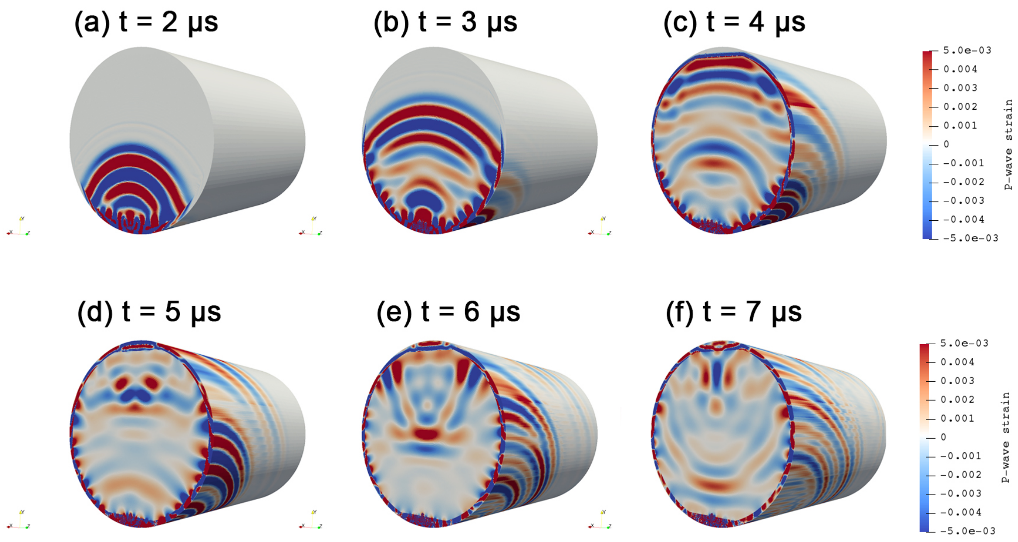

Figure 12. The snapshot of the P-wave wavefield at different time step from 2 to 7 μs, showing P-wave propagation process inside the medium.

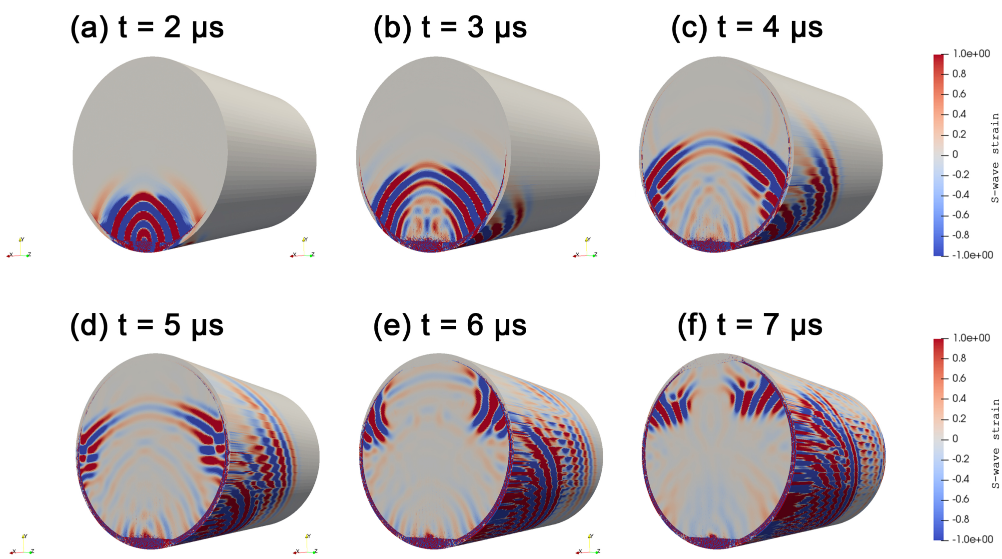

Figure 13. The snapshot of the S-wave wavefield at different time step from 2 to 7 μs, showing S-wave propagation process inside the medium.

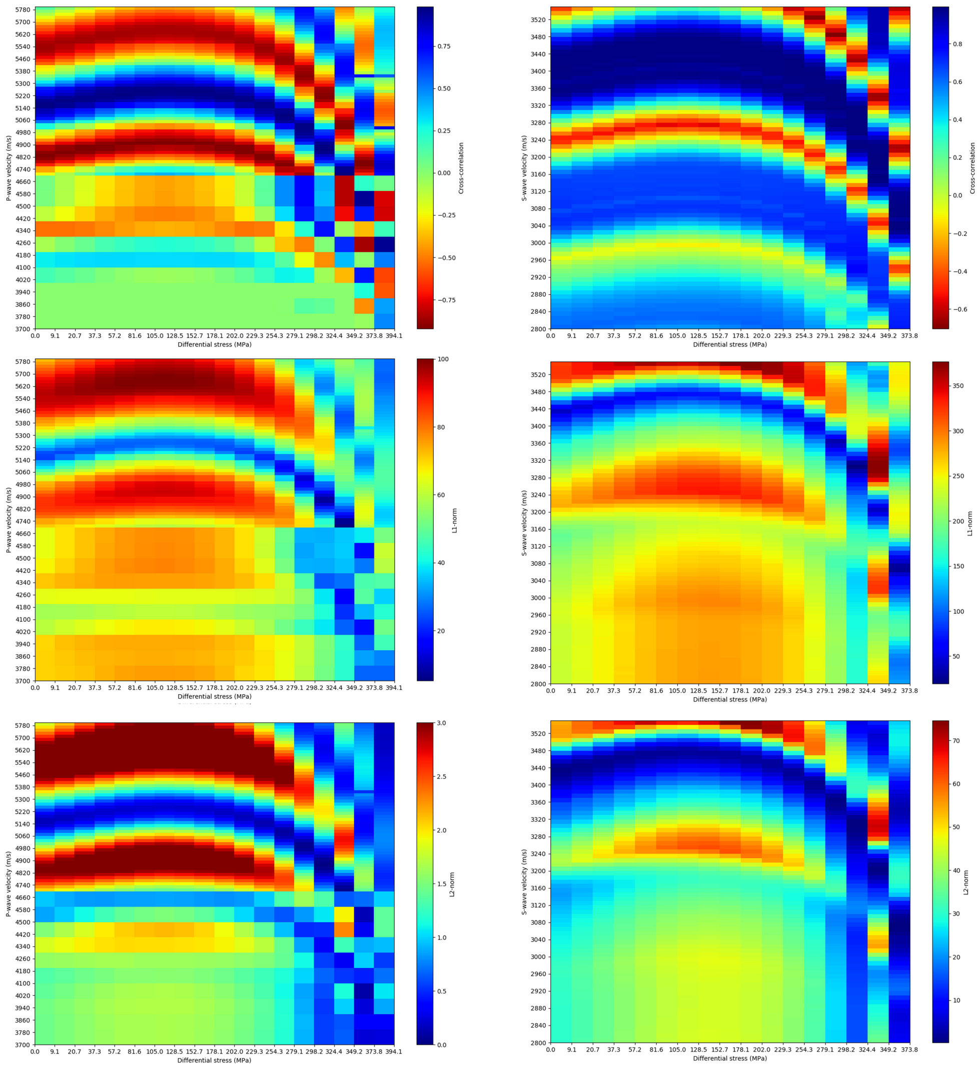

Figure 14. The result of waveform fitting using (top) Zero-lag cross-correlation, (middle) L1-norm, and (bottom) misfit function. The possible trend of change in P-wave (left column) and S-wave (right column)
velocity with increasing differential stress is shown in dark blue.

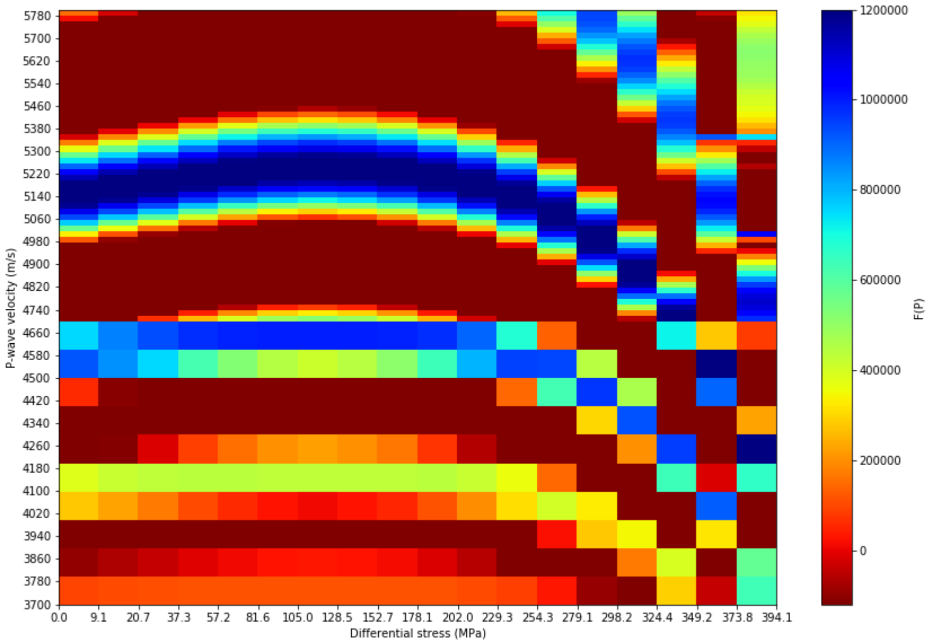

Figure 15. The result of waveform fitting using objective function. The possible trend of change in P-wave velocity with increasing differential stress is shown in dark blue.

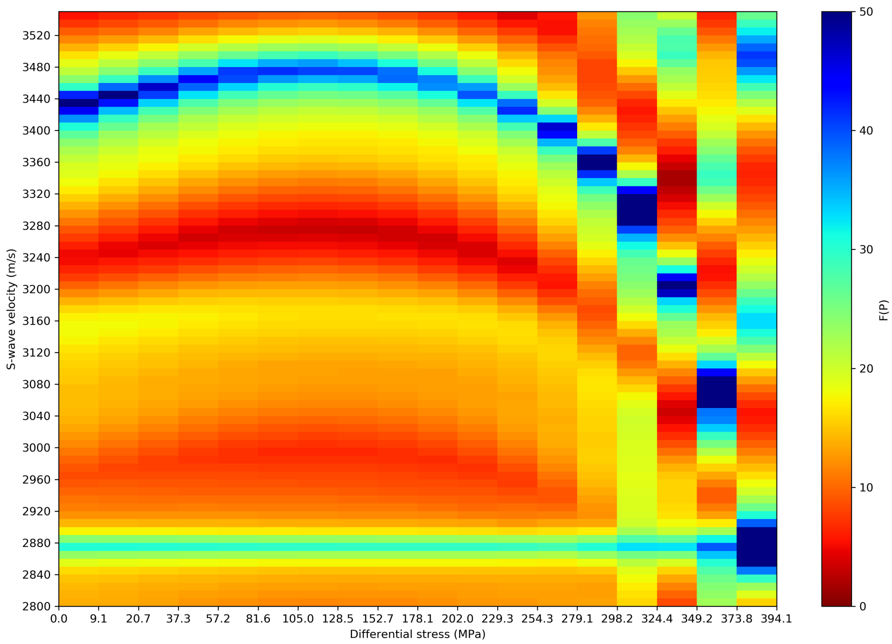

Figure 16. The result of waveform fitting using objective function. The possible trend of change in S-wave velocity with increasing differential stress is shown in dark blue.

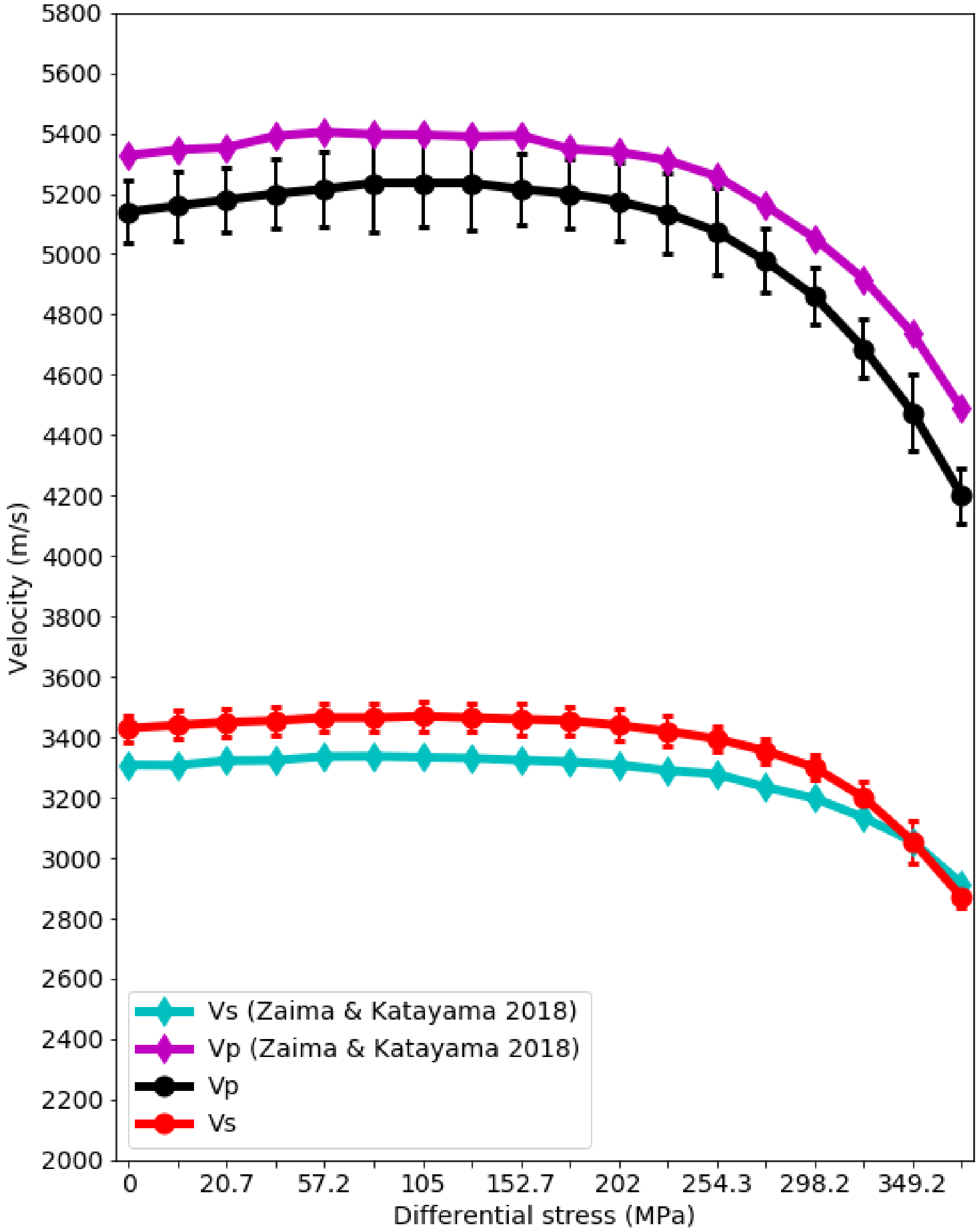

Figure 17. Evolution of V_P and V_S of dry data. The black and red circle represent the numerical simulated best-fit results of V_P and V_S, respectively. The diamond shapes are the results from Zaima and Katayama (2018), which are calculated from the hand-picked first arrivals.

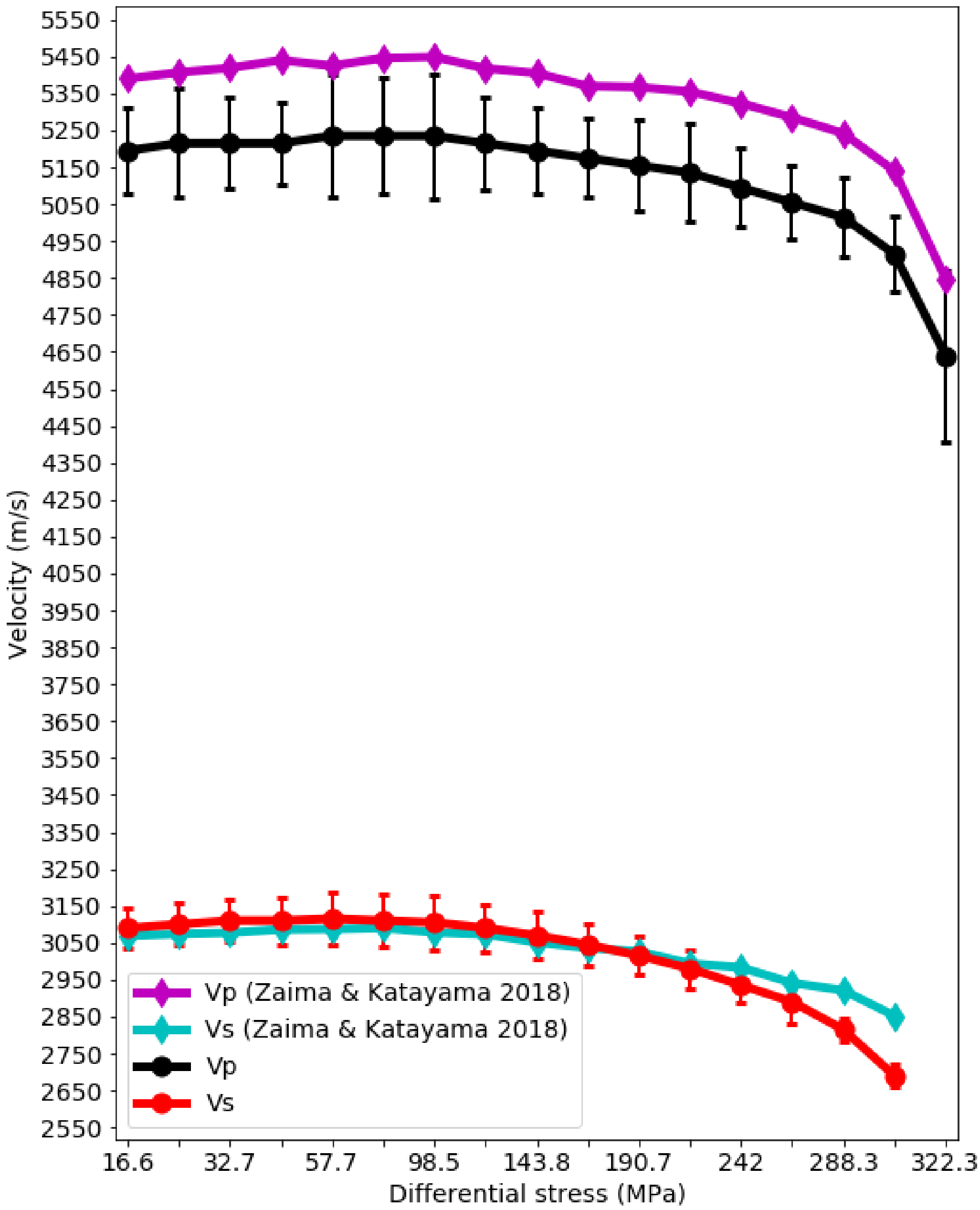

Figure 18. Evolution of V_P and V_S of wet data. The black and red circle represent the numerical simulated best-fit results of V_P and V_S, respectively. The diamond shapes are the results from Zaima and Katayama (2018), which are calculated from the hand-picked first arrivals.

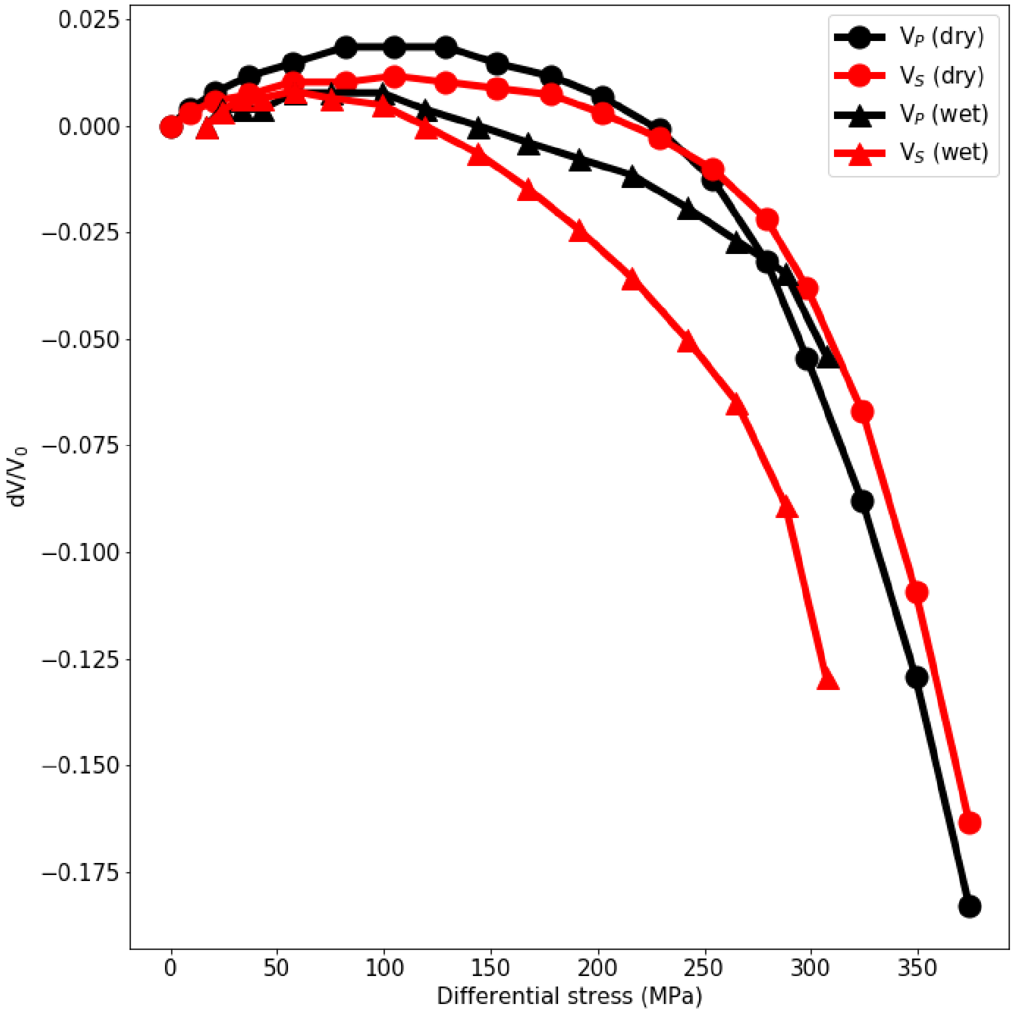

993 **Figure 19.** dV/V_0, showing the velocity change compared to the original stage at each stress
994 condition.

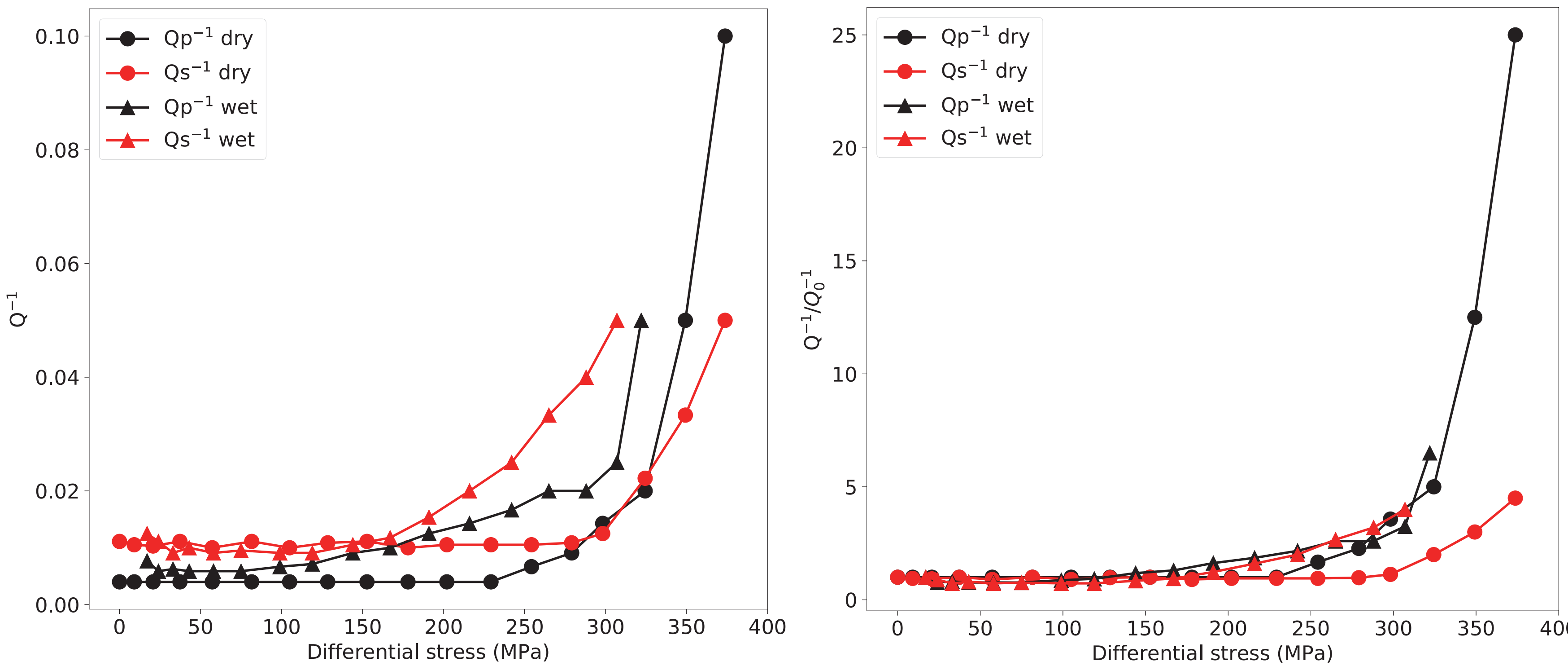

Figure 20. (a) Q^{-1} of wet and dry data, (b) Q^{-1}/Q_0^{-1} of wet and dry data

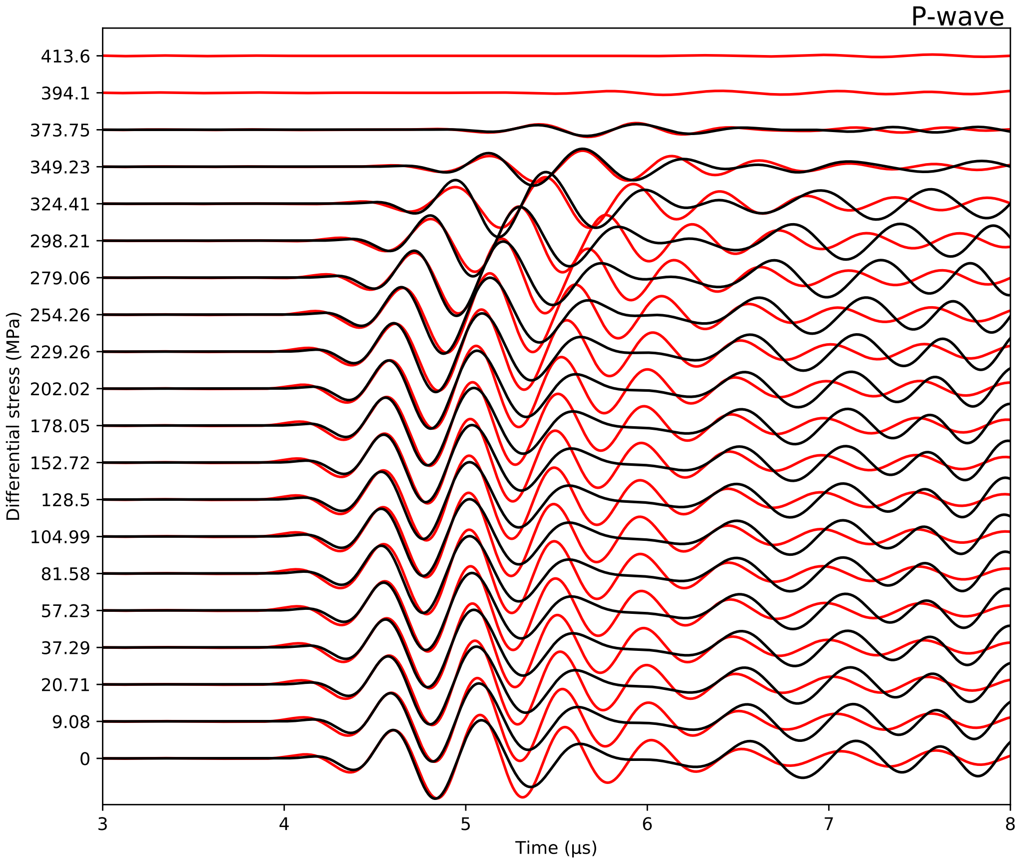

Figure 21. The result of P-wave strain waveform fitting of dry data using equation 3 to find the best-match model with proper V_P, V_S, Q_P, Q_S. The black lines are the best-match synthetic waveforms. The red lines are the experimental data. The y-axis indicate the deformation progress and correspond to a condition of $\Delta\sigma$. The x-axis represents the time of wave propagation.

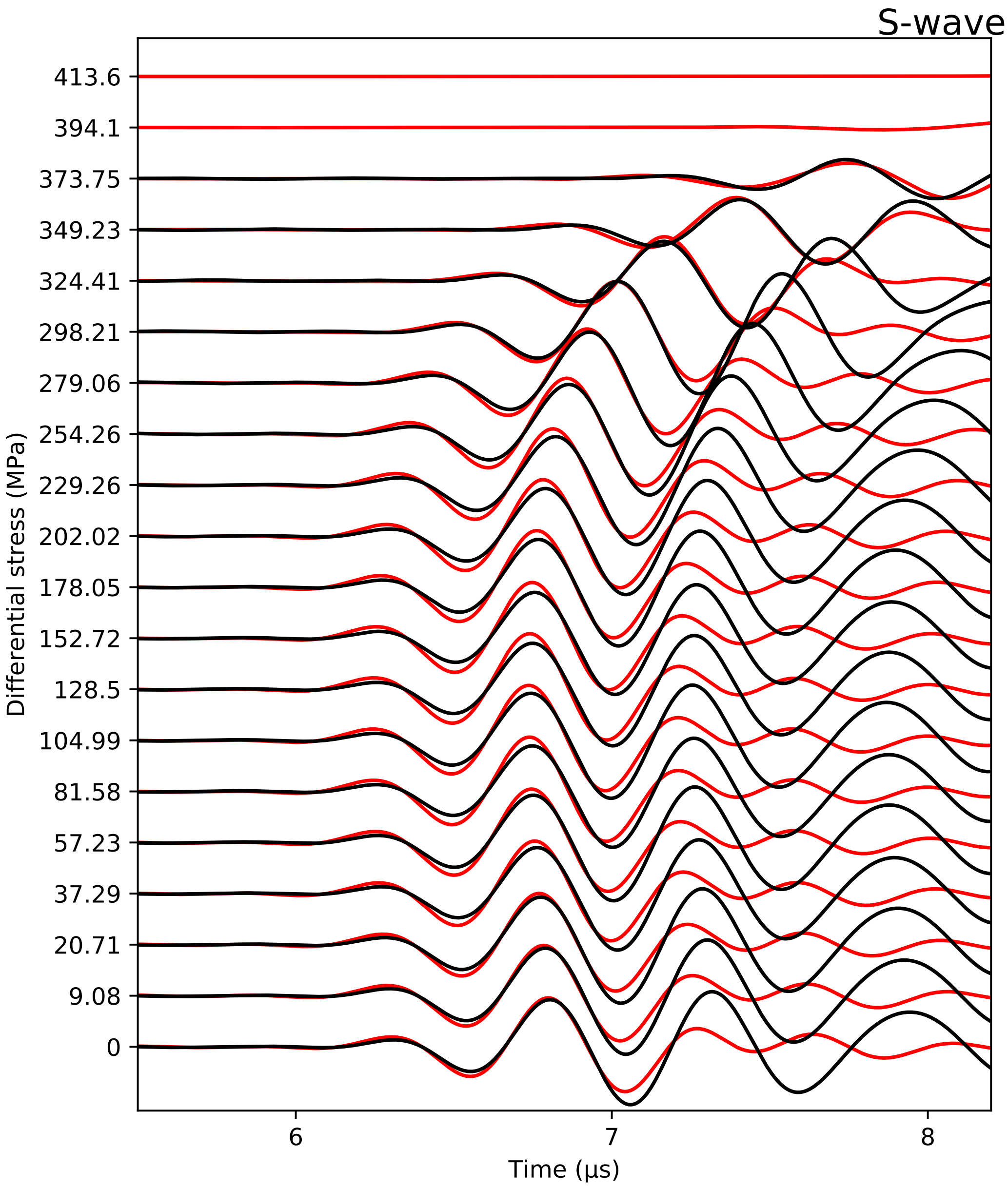

999 **Figure 22.** The result of S-wave strain waveform fitting of dry data using equation 3 to find
1000 the best-match model with proper V_P, V_S, Q_P, Q_S. The black lines are the best-match synthetic
1001 waveforms. The red lines are the experimental data. The y-axis indicate the deformation progress
1002 and correspond to a condition of $\Delta\sigma$. The x-axis represents the time of wave propagation.

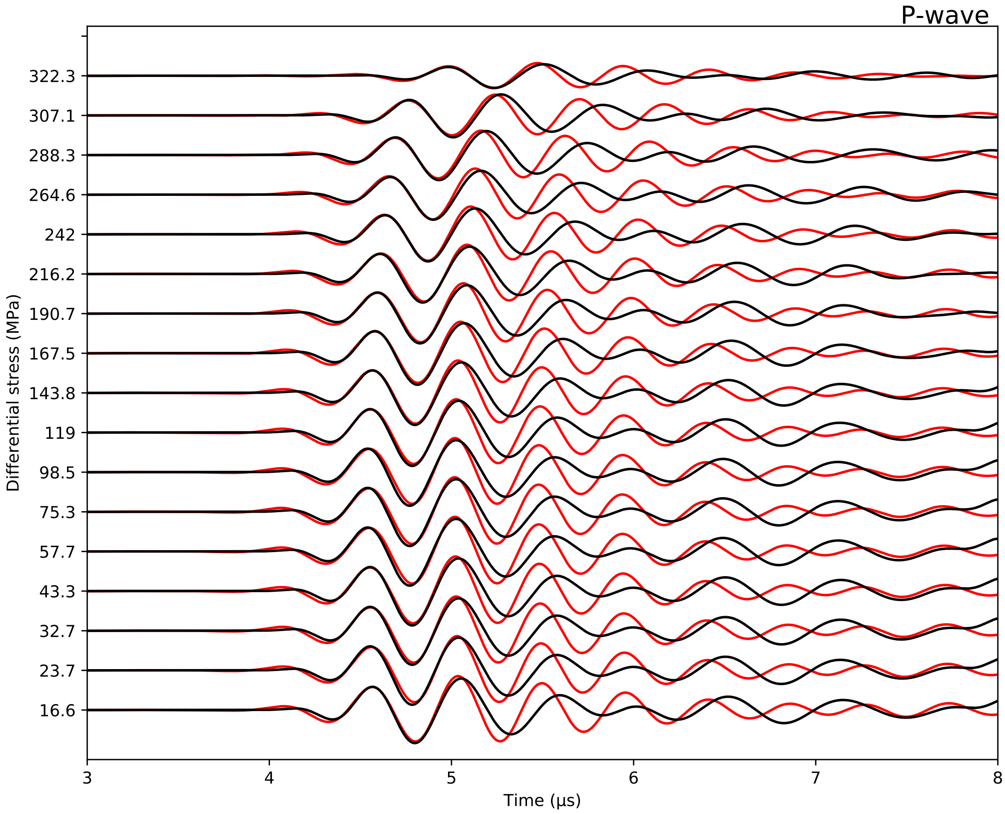

Figure 23. The result of P-wave strain waveform fitting of wet data using equation 3 to find the best-match model with proper V_P, V_S, Q_P, Q_S. The black lines are the best-match synthetic waveforms. The red lines are the experimental data.The y-axis indicate the deformation progress and correspond to a condition of $\Delta\sigma$. The x-axis represents the time of wave propagation.

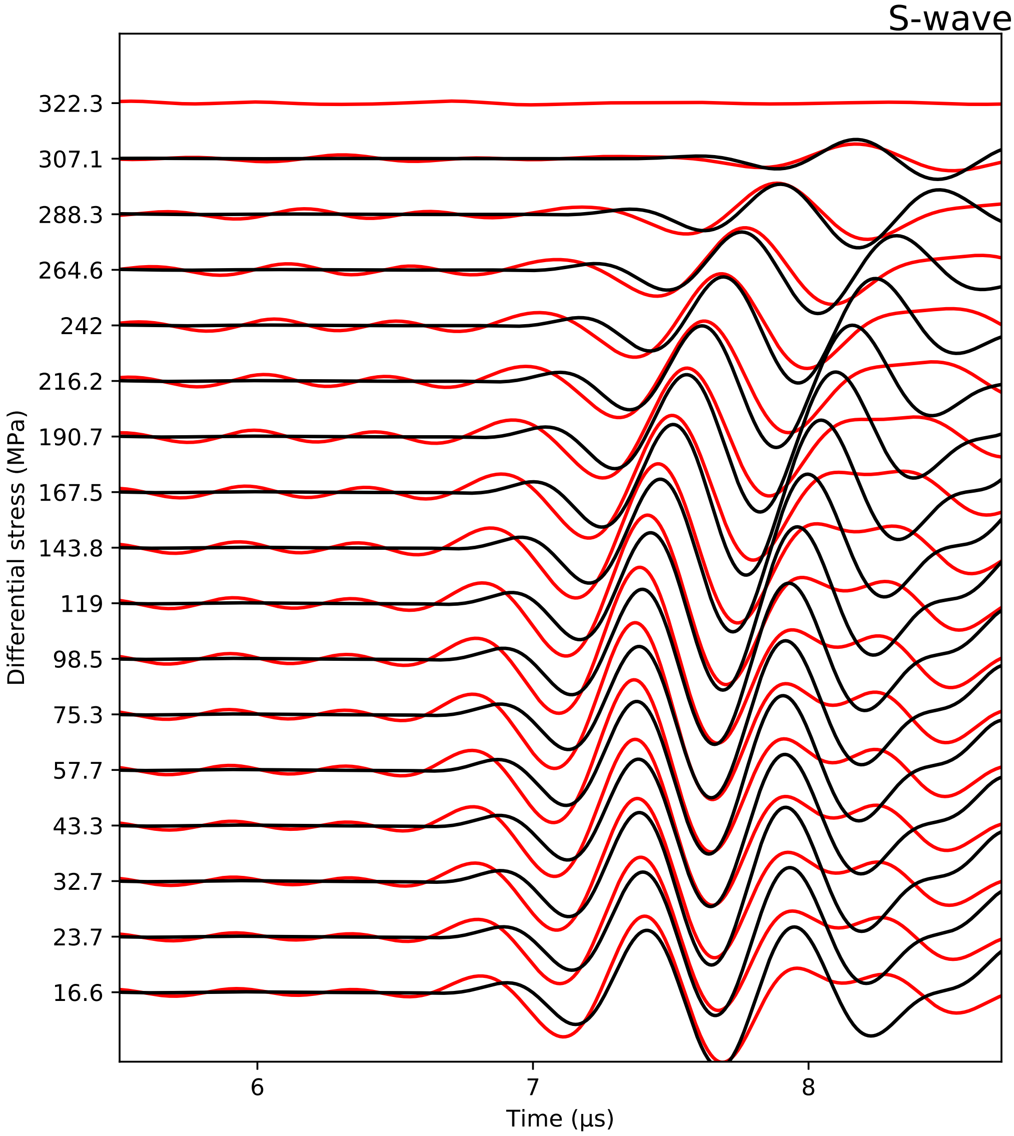

1007 **Figure 24.** The result of S-wave strain waveform fitting of wet data using equation 3 to find
1008 the best-match model with proper V_P, V_S, Q_P, Q_S. The black lines are the best-match synthetic
1009 waveforms. The red lines are the experimental data. The y-axis indicate the deformation progress
1010 and correspond to a condition of $\Delta\sigma$. The x-axis represents the time of wave propagation.

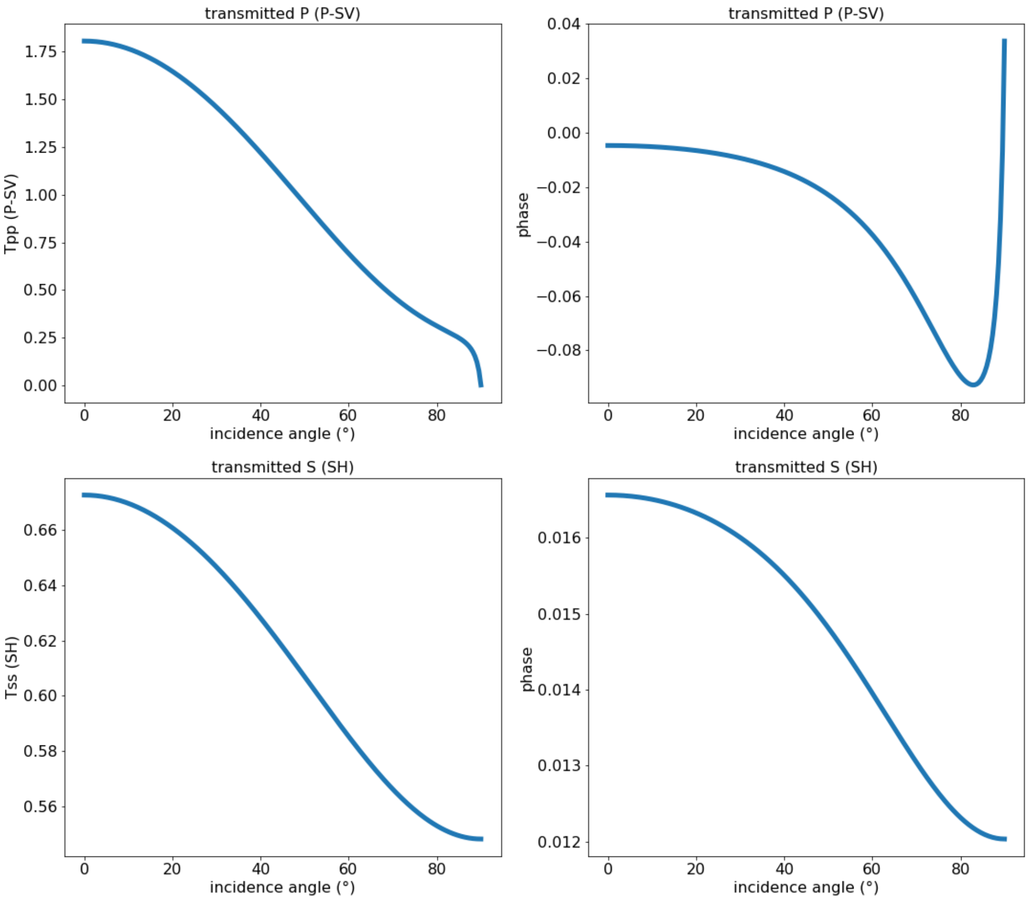

1011 **Figure 25.** The transmission coefficient Tpp (P-SV) and Tss (SH) of solid-solid surface
1012 plotted with incidence angle. (a) Tpp (P-SV) amplitude, (b) Tpp (P-SV) phase, (c) Tss (SH)
1013 amplitude, (d) Tss (SH) phase.

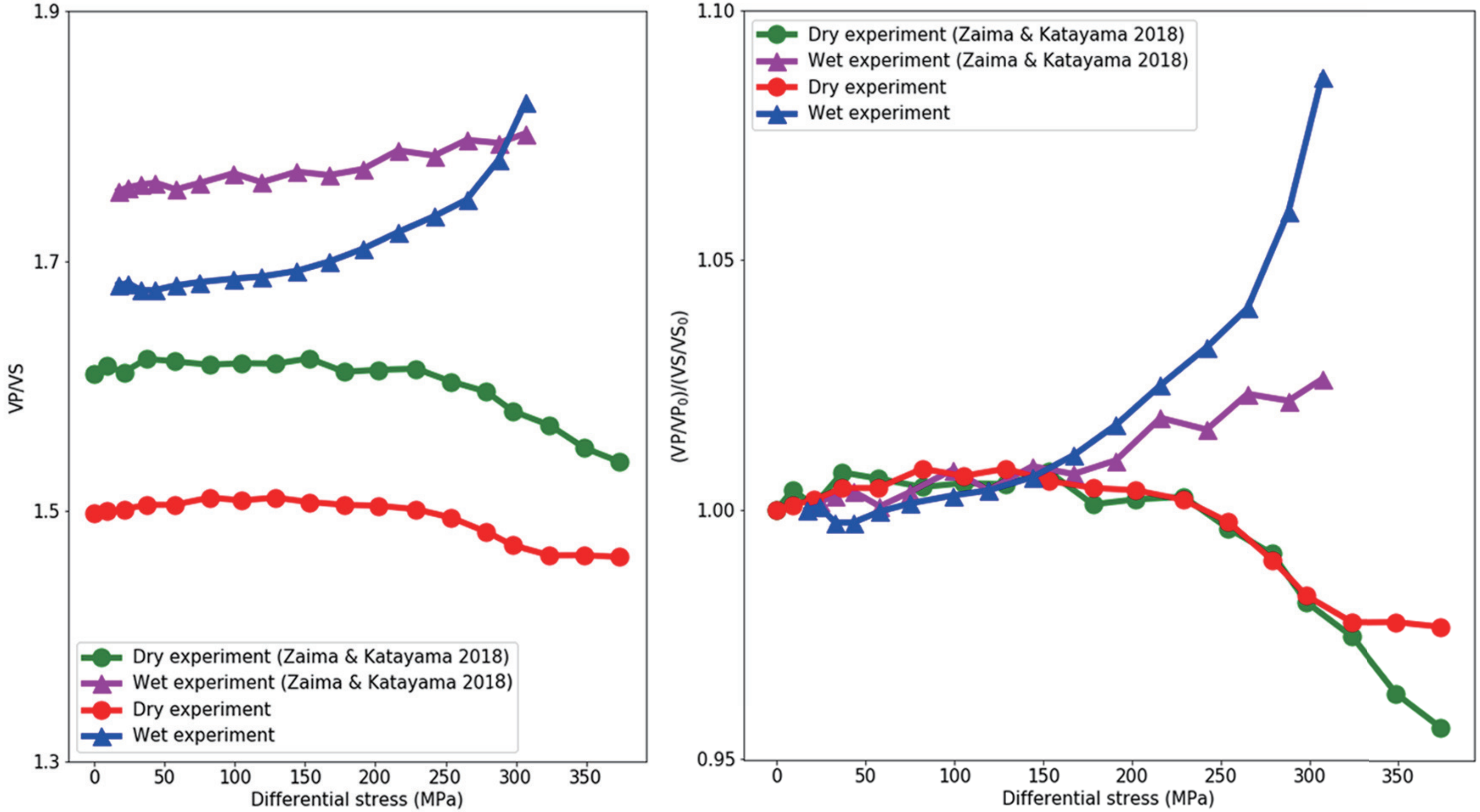

Figure 26. (a)V_P/V_S ratio change, (b)Relative V_P/V_S ratio change.